THE RED MSX SOURCE SURVEY: THE MASSIVE YOUNG STELLAR POPULATION OF OUR GALAXY

S. L. Lumsden[1], M. G. Hoare[1], J. S. Urquhart[2], R. D. Oudmaijer[1], B. Davies[3], J. C. Mottram[4],
H. D. B. Cooper[1], AND T. J. T. Moore[3]
[1] School of Physics and Astronomy, University of Leeds, Leeds LS2 9JT, UK
[2] Max-Planck-Institut für Radioastronomie, Auf dem Hügel 69, Bonn, Germany
[3] Astrophysics Research Institute, Liverpool John Moores University, Liverpool L3 5RF, UK
[4] Leiden Observatory, Leiden University, P.O. Box 9513, 2300 RA Leiden, The Netherlands

ABSTRACT

We present the Red MSX Source survey, the largest statistically selected catalog of young massive protostars and
H II regions to date. We outline the construction of the catalog using mid- and near-infrared color selection. We also
discuss the detailed follow up work at other wavelengths, including higher spatial resolution data in the infrared.
We show that within the adopted selection bounds we are more than 90% complete for the massive protostellar
population, with a positional accuracy of the exciting source of better than 2 arcsec. We briefly summarize some
of the results that can be obtained from studying the properties of the objects in the catalog as a whole; we find
evidence that the most massive stars form: (1) preferentially nearer the Galactic center than the anti-center; (2) in
the most heavily reddened environments, suggestive of high accretion rates; and (3) from the most massive cloud
cores.

Key words: Galaxy: stellar content – infrared: stars – stars: formation – stars: late-type – stars:
pre-main sequence – surveys

Online-only material: color figures, machine-readable table

1. INTRODUCTION

Massive stars play a profound role in the evolution of every
galaxy, but we are still not completely sure how they form.
The origin of this problem goes back to Kahn (1974), who
realized that the radiation pressure from a young massive star
was sufficient to prevent further spherical accretion onto its
surface. The key problem is that a simple scaled-up version
of the low mass star formation model (e.g., Shu et al. 1987)
gives rise to a star in which fusion starts once it becomes more
massive than $\sim$10 $M_\odot$, and hence significant radiation pressure
is inevitable. In addition, massive stars are generally observed
to form in clusters, and always in high density regions, meaning
that the conditions in the molecular cloud in which they form
must be different from those that result in generic, isolated,
low-mass stars.

However, there are several assumptions implicit in these
calculations. First, the calculations ignore the role that accretion
through a disk plays. At high accretion rates, a disk will be self-
shielding against ultraviolet radiation. Secondly, until recently,
few models existed of the properties of massive stars in the
process of formation. It was generally assumed that fusion would
start once the core of the star became massive enough, but this
assumption was never actually tested. The original conclusions
of Kahn (1974), however, have led to many attempts to propose
alternative models for how massive stars form. These alternative
models can be thought of as falling into two classes: those
that attempt to find a modified version of the Shu et al. (1987)
model, by treating disk accretion correctly following monolithic
collapse, and those that propose a completely different mode for
massive star formation.

Recent work on disk accretion has revised the previous
orthodoxy that massive stars cannot form in this fashion. The
high densities and degree of turbulence and short timescales
involved in such regions lead to accretion rates sufficient to
ensure the infalling material overcomes the radiation pressure
(e.g., McKee & Tan 2003). This success led others to attempt
full hydrodynamical models including treatment of the radiation
pressure. One key aspect of all such models is that the collimated
outflows generated in the early stages provide both an escape
route for the radiation and help to sustain the turbulence in the
surrounding cloud. Models by Krumholz et al. (2009, 2010),
using an approximate treatment of the radiation field, found that
the role of the disk and outflow cavity was crucial and that the
higher surface densities in regions of massive star formation
suppress break-up into clusters of smaller stars. Kuiper et al.
(2010) have shown that a full radiative transfer treatment results
in there being essentially no limit on the mass of a star that
can be formed, since the disk effectively self-shields against the
star's radiation pressure. More recently, Kuiper & Yorke (2013)
have shown that gas opacity, rather than dust opacity, above the
disk creates an additional shield so that the "radiation pressure
problem" is reduced even further.

Alternative models for the formation of massive stars still
have some attractive aspects, however. Bonnell et al. (2004)
proposed a mechanism of competitive accretion in which a
cluster forms within a turbulent molecular cloud, with the gas
being fed by dynamical processes toward the center of the cluster
where the most massive star lies. In this model, the mass of the
most massive star is decoupled from the mass of the individual
clump from which it forms. Instead, the mass depends on the
total final cluster mass since it is the lower mass stars that largely
"drag" the gas toward the center. Such a model naturally leads
to the mass segregation seen in actual clusters (e.g., Gennaro
et al. 2011).

The monolithic collapse model predicts increasing accretion
rates with time to form the most massive stars, as does the
competitive accretion model. These models do vary in other
aspects, however (e.g., location of the most massive accreting
star in a cluster, the temporal sequence of star formation

throughout a cluster, etc.). Only a large observational sample will clearly discriminate among these models.

Another recent theoretical development was the modeling by Hosokawa & Omukai (2009) and Hosokawa et al. (2010) of the internal structure of massive stars as they are forming. These authors show that hydrogen fusion is delayed until the star has grown to about 10 $M_\odot$ at high accretion rates ($\gtrsim 10^{-4}$ $M_\odot$ yr^{-1}). Before that time, a combination of deuterium burning and accretion luminosity is largely dominant. Furthermore, the star remains relatively deficient in ultraviolet photons until accretion is almost over, since the natural configuration for a star that has considerable mass (hence entropy) being loaded onto it is to swell up into something resembling a cool supergiant, a consequence that had previously also been discussed by Hoare & Franco (2007) in the context of the lack of H II regions around massive protostars. This result also helps to alleviate any remaining issues with the problem of radiation pressure in theoretical models for massive star formation.

Though much still remains to be clarified (e.g., the role of magnetic fields), the theoretical picture is at least clearer now. The greatest limitation therefore is a lack of suitable observational data, especially in a statistical sense. There is a clear need therefore for a comprehensive study of the young massive star population in our Galaxy. The ideal means of identifying young and forming massive stars is through a combined far- and mid-infrared survey, since those wavelengths are where the bulk of the stellar emission is re-radiated. Unfortunately, existing published data covering a significant fraction of the Galactic plane are either of low spatial resolution (e.g., *IRAS*: cf. Chan et al. 1996 or Campbell et al. 1989) or lack the dynamic range required to study a wide mass range (e.g., GLIMPSE: Benjamin et al. 2003, Churchwell et al. 2009; MIPSGAL: Mizuno et al. 2008, Carey et al. 2009). The former means it is difficult to clearly attribute luminosities to sources in crowded region such as the inner Galactic plane and the latter makes it impossible to create a survey ranging from the highest masses down through mid-B stars, without the former saturating on the initial images. Future catalogs based on *Herschel* (e.g., HiGAL; Molinari et al. 2010) will alleviate both these limitations in the far-infrared and sub-mm regimes, but such surveys cannot truly determine source properties without additional shorter wavelength data.

Instead, as reported in Lumsden et al. (2002), we adopted a strategy of combining mid-infrared data from the *Midcourse Space Experiment* (*MSX*) satellite mission and ground-based near-infrared photometry from the Two Micron All Sky Survey (2MASS) to characterize the properties of the mid-infrared population of the Galactic plane. A protostar becomes a bright thermal infrared source even at a relatively early stage due to the luminosity from contraction and accretion. At this point, dust is heated to >200 K, which primarily leads to emission beyond 5 μm. Hence, mid-infrared selection is a viable means of detecting most of the population Galaxy-wide. We include those highly reddened sources that are either not detected at all in the near-infrared or else only detected at one band, in a fully self-consistent fashion in order to ensure we include the most embedded sources. *MSX* has superior spatial resolution to *IRAS*, but is obviously worse than what is achievable with *Spitzer*. *MSX* is, however, insensitive to saturation for the objects we are studying, unlike, say, *Spitzer*. The *MSX* point source catalog (PSC; Egan et al. 2003) is therefore likely to be more complete, without considerable additional effort, than other currently existing public catalogs for the most massive stars. We

are primarily interested in how these stars form and therefore *MSX* is a natural choice as a starting point. The use of a single initial catalog is also very attractive from the point of view of statistical studies. All of our final classifications are based on the acquisition of higher spatial resolution data in the thermal infrared so the spatial resolution of *MSX* is not a fundamental drawback. The *MSX* data therefore have the capacity to create a preliminary catalog from which we draw all the young high-mass objects through extensive further follow-up work, which has taken place over the last 13 yr. As we noted in Lumsden et al. (2002), different classes of mid-infrared bright objects segregate rather well in the combined *MSX*/2MASS color space.

In this paper, we publish our combined catalog, including details of all the follow-up studies carried out. We discuss the completeness, astrometric accuracy, classification criteria, and briefly outline some areas of science where the catalog as a whole can help to address issues in massive star formation.

2. CONSTRUCTION OF THE CATALOG

2.1. The MSX Point Source Catalog

The *MSX* satellite mission included an astronomy experiment (SPIRIT III) designed to acquire mid-infrared photometry of sources in the Galactic plane ($b < 5°$). *MSX* had a raw resolution of 18″.3, a beam size 50 times smaller than that of *IRAS* at 12 and 25 μm. *MSX* observed six bands between 4 and 21 μm, of which the four between 8 and 21 μm are sensitive to astronomical sources. Full details of the mission can be found in Price et al. (2001). We used v2.3 of the *MSX* PSC (Egan et al. 2003) as our basic input, restricting ourselves to the main Galactic plane catalog, which excludes sources seen in only a single observing pass and those seen in multiple passes but with low significance. The most sensitive data, by a factor of ~10, were acquired using an 8.3 μm filter (band *A*: bandwidth 3.4 μm). As a result, many objects are detected only in band *A*; the vast majority of these are normal stars (see, e.g., Clarke et al. 2005). The point source sensitivity of band *A* was similar to that of the *IRAS* 12 μm band, about 0.1 Jy (Egan et al. 2003). Data obtained using both the 14.7 and 21.3 μm filters (bands *D* and *E*: widths 2.2 and 6.2 μm, respectively), although less sensitive, were also of particular value to us since we are primarily interested in red objects.

We restricted our catalog to $10° < l < 350°$ in order to avoid problems with greater source confusion, as well as kinematic distance ambiguities near the Galactic center. Since we are searching for red objects, our final limiting sensitivity is that imposed by band *E*. This sensitivity varies as a function of position in the Galaxy (Egan et al. 2003; Davies et al. 2011). Egan et al. find a 90% completeness limit of 1.5 Jy for the main *MSX* point source catalog as a whole. The distribution of band *E* fluxes for the region of the plane we are considering is shown in Figure 1. The turn-over in the number counts lies at ~2.5 Jy, with reliable 95% completeness at ~2.7 Jy (assuming the data follow a power law as a function of flux). We have adopted 2.7 Jy as the limit for our catalog. The upturn in the data below 1.5 Jy is due to detection of sources in regions of greater sensitivity (the CB03 regions, as described by Egan et al. 2003). These regions are limited in extent and therefore do not influence the limiting sensitivity of the plane survey as a whole.

Our final master list consists of those sources with quality flags of 2 or greater in band *E* (which nominally corresponds to a signal-to-noise ratio greater than 5) and a detection in at least one of bands *A* and *D*, satisfying our color criteria. Where
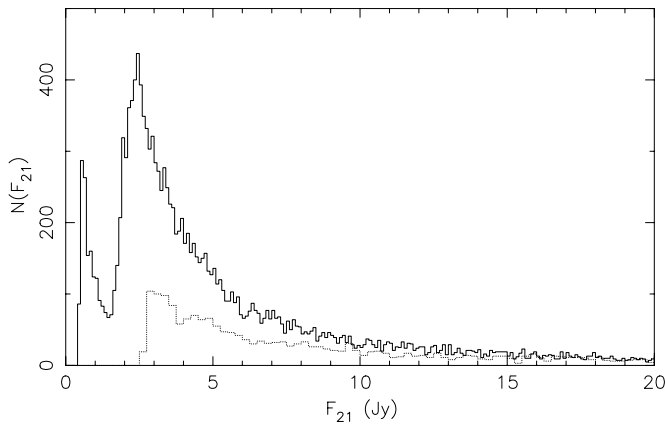
Figure 1. Distribution of the 21 μm fluxes for all *MSX* point sources contained in version 2.3 of the catalog in bins of 0.1 Jy. The dotted line shows the distribution of fluxes for all those sources confirmed by us to be point sources that satisfy our other selection criteria for red sources, but with a coarser bin width of 0.25 Jy.

only one detection in either band *A* or *D* exists, we use the upper limit on the other to ensure that the limit satisfies the color selection. The final color criteria that we apply to the *MSX* catalog are $F_E > 2F_A$ and $F_E > F_D$, as we discuss in Section 2.5. We adopt conservative boundaries in defining all the color cuts we use, whether mid- or near-infrared, by including all objects whose error bars permit them to possibly lie within the boundary. The main consequence of this procedure is that we include a significant number of faint evolved stars in our final sample that lie on the blue side of the boundary, as is evident from the color–color plot shown in Figure 2. In total, after the *MSX*-based color cuts, there are 4013 objects that satisfy our band *E* cut that also have detections in bands *A* and *D* with quality $\geqslant 2$. Another 226 objects are detected in bands *E* and *A* with similar flags, but formally not detected in band *D*. Furthermore, 412 objects are detected in bands *E* and *D*, but not band *A*. We merged all of these objects together into a master list containing 4651 objects.

Hereafter, we will refer to *MSX* bands *A*, *D*, and *E* by their central wavelengths as the 8, 14, and 21 μm bands in this paper for simplicity.

2.2. Extended Source Rejection

The *MSX* PSC contains many red sources that are not genuine point sources. The catalog parameters do not necessarily indicate where such extended objects exist in a reliable fashion. A visual inspection of the *MSX* images revealed that $\sim$1/3 of our candidates were more extended than 36 arcsec. Of course, the sizes of these sources can only be determined accurately using higher resolution data, especially in regions where multiple real sources exist and combine to form one *MSX* source. Acquisition of higher spatial resolution mid infrared imaging was a key part of our survey, and we used these data in this visual rejection of very extended sources. In practice, this employed a combination of our own ground-based, mid infrared imaging (Mottram et al. 2007), as well as archival *Spitzer* data (specifically data from the *Spitzer* Glimpse Legacy Survey are used extensively (Churchwell et al. 2009) as well as other archival *Spitzer* data where they exist). In a few cases, when neither of these data types exist, we recently revisited this issue by examining data from the *WISE* satellite (Wright et al. 2010).

The complex emission present in some of these regions made it simpler to check source sizes manually than to use an automated process. The natural drawback to this method is that the final selection is prone to human error in the classification. In order to try and prevent the latter from significantly affecting our catalog, we only excluded objects that were extended beyond approximately two *MSX* beamwidths. These sources fall into two types, as described below.

The first are genuine, internally illuminated, extended H ɪɪ regions, which we list in our catalog as "Diffuse H ɪɪ Regions." Our catalog is not complete for such objects. Sometimes very extended objects are split into more than one source by the *MSX* point source finding algorithm. In such cases, we have kept only a single final source. We note, however, that the astrometry of such sources is particularly poor and we have not attempted to improve on the original *MSX* coordinates. We have identified

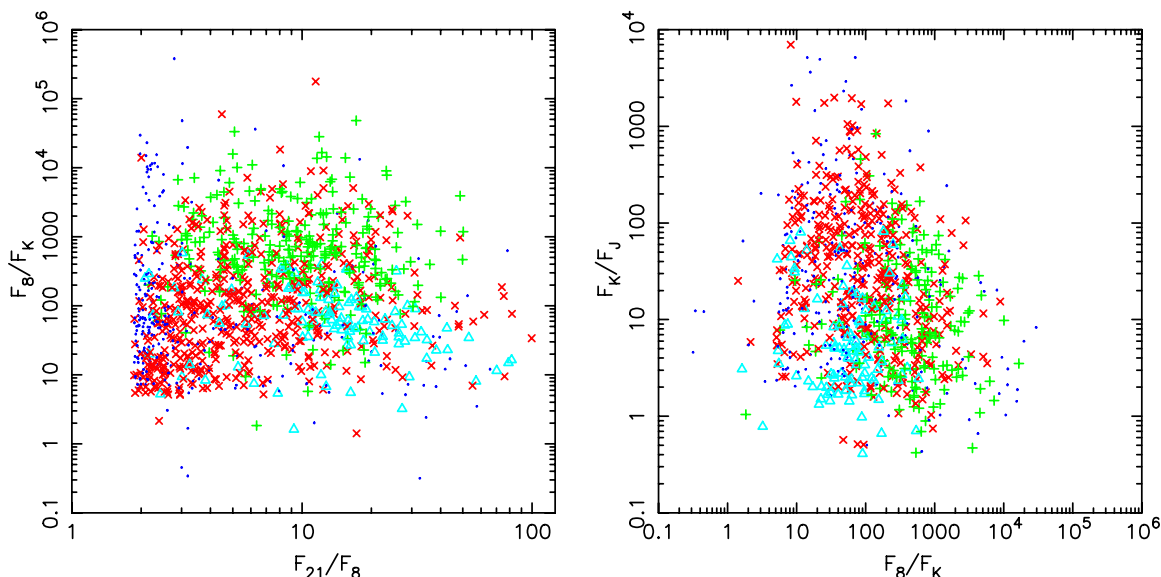**Figure 2.** Color–color distribution of YSOs ($\times$s; colored red in the online version), H ɪɪ regions (+s, colored green in the online version), PNs (triangles; colored cyan in the online version), and evolved stars (dots; colored blue in the online version). The classifications are taken from the work described in Section 2.6.

(A color version of this figure is available in the online journal.)

620 sources classified in this way. These diffuse H II regions are retained in the final catalog, although in general we do not study them further.

The second type of objects is actually rejected from the master list since they appear to be extended background or filamentary emission around much larger structures or artifacts due to the presence of nearby bright sources. There are 1501 such sources. Emission of this kind naturally belongs to the larger source and is not a point source on its own. Such sources tend to cluster in particular around sites of known extended star formation (e.g., the Carina nebula). In these regions, it appears the *MSX* point source detection algorithm is not reliable. For the same reason, we are probably missing genuine point sources in such areas, especially closer to the brighter central regions. In Davies et al. (2011), we attempted to quantify this effect by randomly placing point sources into the original *MSX* image tiles and then recovering them using a similar algorithm to the *MSX* PSC. The result is that our final catalog completeness is actually position dependent on the sky. Davies et al. factored this result into their statistical analysis of the catalog.

Finally, visual inspection of high-resolution, mid-infrared data allows us to identify the main counterpart of the *MSX* source correctly and hence improve on the *MSX* astrometry, as well as addressing the issue of source multiplicity. We will return to this issue in Section 2.4. Perhaps most crucially, this check also allows us to identify compact clusters of exciting sources. Hereafter, we only consider those 2539 objects that pass the requirements that any candidate has at least one red compact source present in the *MSX* beam.

2.3. Near Infrared Counterparts

The only available suitable all-plane survey in the near-infrared is 2MASS (Skrutskie et al. 2006). We utilized the data from both the 2MASS Point Source Catalog (2MASS PSC) and the Extended Source Catalog. The 2MASS detectors are limited at bright magnitudes by saturation, but fluxes in the PSC are derived from fits to the wings of the point spread function; this technique reduces that limitation to a handful of very bright stars. At faint magnitudes, the 2MASS PSC is, however, close to confusion limited in many areas of the Galactic plane.

We have also now added deeper infrared imaging data to our database where available. These data come from two surveys, the UK Infrared Telescope (UKIRT) Infrared Deep Sky Survey (UKIDSS) Galactic Plane Survey (Lucas et al. 2008) and the Vista Variables in the Via Lactea (VVV) survey (Minniti et al. 2010), both of which are deeper and have better spatial resolution than 2MASS. UKIDSS uses the UKIRT Wide Field Camera (Casali et al. 2007) on UKIRT, and VVV uses the Visible and Infrared Survey Telescope for Astronomy.

The UKIDSS project as a whole is defined in Lawrence et al. (2007). The pipeline processing and science archive for UKIDSS/VVV are described in Hodgkin et al. (2012) and Hambly et al. (2008). For the data used in this paper, a similar procedure was in use for VVV (Lewis et al. 2010). The photometric system of UKIDSS is described in Hewett et al. (2006) and the calibration is described in Hodgkin et al. (2009).

There are relatively minor differences in the *J*- and *H*-band photometry between 2MASS and UKIDSS/VVV, but the difference is more substantial in the *K*-band where both 2MASS and VVV use a similar K_s filter and UKIDSS uses a more traditional *K* filter that additionally permits the transmission of light in the $\sim$2.3–2.4 μm range. The color terms to translate these data back into the 2MASS system are known for relatively unreddened stars (e.g., Hodgkin et al. 2009), but rely on having accurate *J*-band 2MASS data, which are not available for many of our very red sources. We have considered the color term for all unsaturated *K*-band sources with UKIDSS and the results are shown in Figure 3. The majority of our sources are consistent with only a small color term of $\sim$0.2$(J - K)$ being required to place the UKIDSS data fully in the 2MASS system. Since the errors in the magnitudes in these regions tend to be as large as this small correction, we have ignored these corrections in what follows.

We also plot the global comparison of the 2MASS data with the combined UKIDSS/VVV data in Figure 3. The 2MASS data will always be preferable for very bright objects since the UKIDSS and VVV cameras saturate near 10th magnitude in all bands, as can be seen in the figure. There also exists a substantial group of objects for which the data differ by more than the nominal errors on either set. This group largely comprises objects that are blended with either other stars or nebular contamination in 2MASS, although there is a subset that are actually fainter in the 2MASS survey. Some of these differences are due to saturation effects in the UKIDSS/VVV data and other objects are moderately extended H II regions in the near-infrared, so the cataloged magnitudes depend largely on the measurement method. In practice, we do not include near-infrared data for clearly very extended objects such as most of the H II regions in our analysis. There are also occasional examples of stars that would appear to be extremely variable (e.g., the low mass young stellar object (YSO) G338.5459+02.1175 has genuinely become 100$\times$ fainter between the 2MASS and VVV observations). These exceptions also help to explain the presence of unusual objects in the comparison of 2MASS and UKIDSS photometry as a function of UKIDSS color. Wherever possible in the final catalog, we have adopted the UKIDSS/VVV data, where they exist, for sources with 2MASS magnitudes fainter than the saturation limits. In other cases, we have adopted the 2MASS data.

The actual near-infrared counterpart selected is based on the coordinates derived from the mid-infrared astrometry (see Section 2.4). We selected the best match based on a visual comparison of the mid- and near-infrared data. Some objects have no direct counterpart, since they are obscured even in the *K*-band, although extended emission such as reflection nebulosity may be present. All these objects are guaranteed to be sufficiently red to satisfy the color criteria described in Section 2.5. Of course, this matching still leaves the possibility that some of our sources are not visible in the near-infrared and that we have picked a neighboring near-infrared source that has a chance alignment with the real target, given the resolution of the data. This fact may be especially true in massive star forming regions where dense clusters of associated stars are present (e.g., Carpenter et al. 1993; Hodapp 1994) and in some cases the true massive young stellar object (MYSO) may be completely obscured. Such dense clusters however appear to be rare in our sample, and we are therefore confident that the number of incorrectly attributed near-infrared fluxes remains small.

We can partly quantify these effects. We identified all 2MASS sources within a 5 arcsec radius of the 2539 sources that passed the checks discussed in the previous section. These sources include many objects, such as most H II regions, where there is no clear counterpart near the center. The number of false associations can be estimated by extrapolating back the number seen at larger separations, which are all presumed to be chance coincidence, to those within 1 arcsec. The net result is that
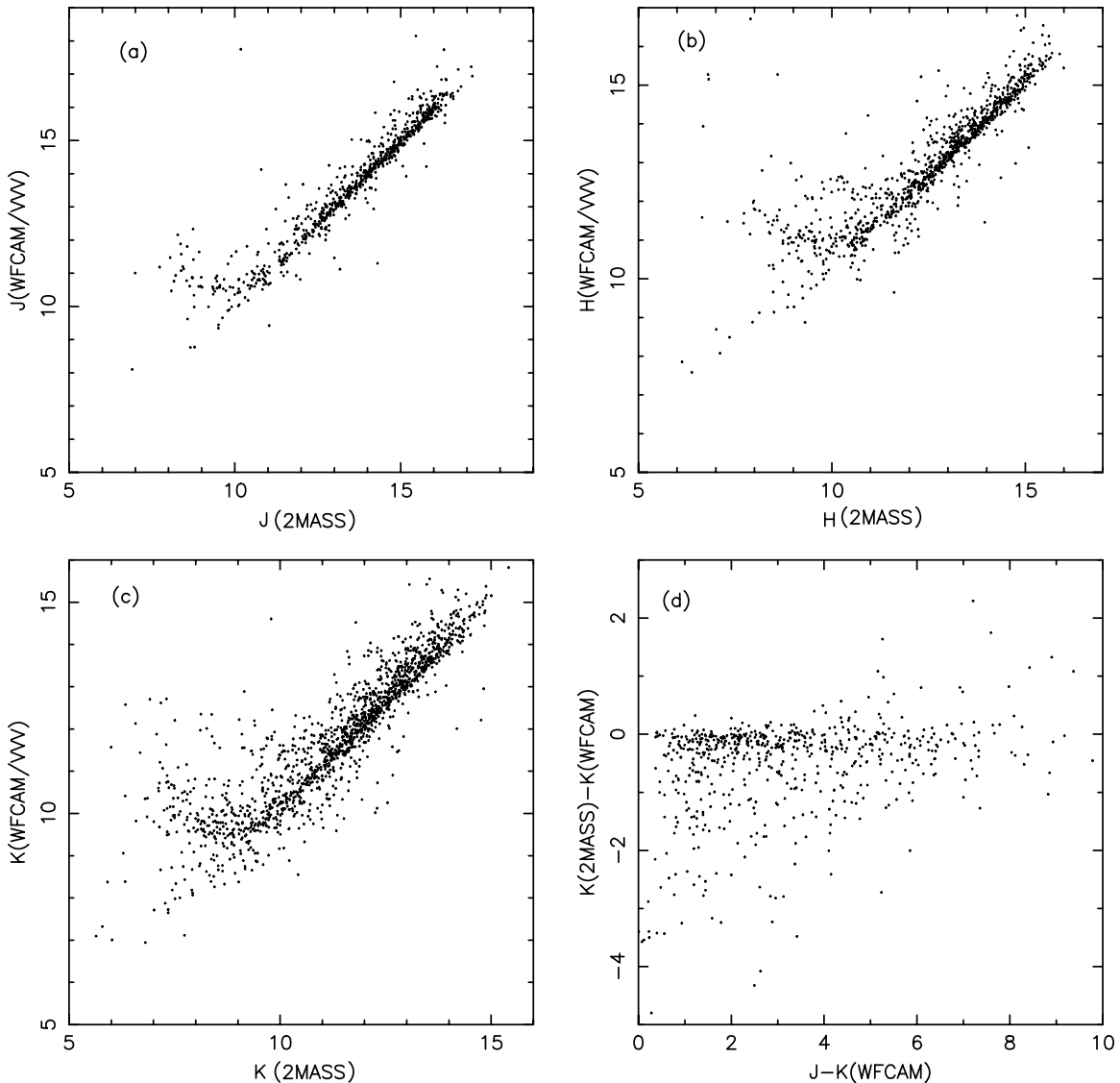
Figure 3. Comparison of 2MASS and UKIDSS or VVV magnitudes, for the *J*-band (a), the *H*-band (b), and the *K*-band (c). The final panel (d) shows the color term involved in comparing UKIDSS and 2MASS magnitudes in the *K*-band.

perhaps 10% of the counterparts should be seen by chance within 1 arcsec. This fraction drops to about 2% within 0.5 arcsec. Our typical astrometric accuracy from the mid-infrared lies in this range for point sources. We have excluded any near-infrared counterpart that lies outside this range as being a likely chance coincidence. The actual ratios are remarkably similar when we consider the deeper UKIDSS data, with 15% expected by chance within 1 arcsec and 3% within 0.5 arcsec. The UKIDSS/VVV astrometry is accurate enough such that we can match objects within the smaller radius. Finally, we should note that every counterpart has been visually inspected to ensure that the identification is sensible. Where the alignment appears to be due to chance (e.g., a very blue star with a very red thermal infrared source), we have excluded the cross-match. Overall, we expect that this procedure leaves us with no more than 5% incorrectly identified counterparts.

2.4. Astrometry

The general astrometry of the *MSX* point source catalog is discussed by Egan et al. (2003). Improvements were made to the earlier version of the *MSX* PSC that resulted in reasonably accurate positions of isolated point sources. Issues still arise near very bright sources, as discussed in Lumsden et al. (2002). However, the main concern with the astrometry lies in crowded regions. We have checked the basic reliability for point sources in several ways. The most uniform comparison, in the sense that it covers all of our Red MSX Sources (RMSs), was with the all-sky *WISE* survey, which matches the longer wavelength range of *MSX* but with a better spatial resolution (12 arcsec at 25 μm and 6 arcsec at all the shorter wavelengths). *WISE* suffers from saturation for bright sources and the fact that the published catalog is described as a source finding catalog rather than a point source catalog (Cutri et al. 2012). Nonetheless, we have cross-correlated the original *MSX* and *WISE* catalogs for point sources that are fainter than the absolute *WISE* saturation limit (about $F_{25} = 330$ Jy). We first considered the positions of evolved stars, which tend to be isolated; 99.5% of the sources have positions that agree within 5 arcsec and 80% agree within 2 arcsec. For all sources (excluding diffuse H II regions and those rejected during visual inspection) the equivalent figures are 9.5 and 3.5 arcsec, respectively. Excluding those H II regions that

are resolved by *WISE* but not strongly resolved by *MSX* reduces these values by 0.5–1 arcsec. Most of the difference between the values for the evolved stars and other sources arises due to source multiplicity in crowded regions—all such regions are associated with star formation.

It is clear, therefore, that we require improved astrometry to accurately identify counterparts. This identification is not possible to do at a long enough wavelength such that we are sampling near the peak of the spectral energy distribution, but it is possible to use thermal infrared images to identify counterparts; shorter wavelength data can then be used to improve the astrometry in most cases. The main surveys used to improve the accuracy of the astrometry in this way were the *Spitzer* GLIMPSE, 2MASS, UKIDSS, and VVV surveys, as well as radio images taken during the construction of this catalog. Finally, if other options proved unsuitable, the *WISE* survey or *Spitzer* MIPS images were employed.

As the above discussion demonstrates, there is generally more than a single source that is bright at thermal infrared wavelengths in star forming regions; there is typically significant extended emission as well. Our aim was to identify all significant compact sources present within, or very close to, the *MSX* beam that can contribute to the total 21 μm luminosity. These "multiple sources" are separated in our online catalog, with the astrometry measured as for other objects. The luminosity for each individual source is estimated using the highest spatial resolution thermal infrared data. These correction factors are all listed in the online version of our catalog. There are a few exceptions to this process. Extended H II regions can have rather irregular morphologies, and it is difficult to determine whether there is only one region present. We also ignore any sources in the field that are "blue" since they will contribute relatively little to the far infrared luminosity. Finally, we have not separated sources where more than one evolved star is present, as these are not of primary interest to us. We have tried to separate all sources where a YSO is present with either another YSO or an H II region, however. The catalog currently contains 216 original *MSX* candidates that have been separated in this fashion.

The process of choosing the best astrometry varies slightly with source type. Where the target shows a clear point source in GLIMPSE or an equivalent survey, we have adopted that position. Where *Spitzer* data are unavailable, we have matched the thermal infrared information we do have (either our own or based on *WISE*) to select potential near-infrared counterparts if these exist. We note that we only use such near-infrared data where we can locate the source with reasonable accuracy from the thermal infrared—near-infrared data on their own are unlikely to be entirely accurate as we may instead choose a reflection nebulosity as the center where a very obscured source is hidden from our line of sight. We only use *WISE* or MIPS data for point source astrometry when these conditions are not met. For H II regions or planetary nebulae (PNs) that are compact, we adopt the same procedure, unless they are detected in the radio. In that case, we adopt the radio position. Weak, irregular, and large H II regions pose a particular challenge as they have no clearly defined center. In such circumstances, we adopted the flux-weighted centroid from GLIMPSE, *WISE* or MIPS data if that is feasible, or else we mark the center using the position of the apparent exciting star(s). The accuracy of such results for these extended sources may only be good to 2–3 arcsec, but is generally better than the accuracy of the initial *MSX* data.
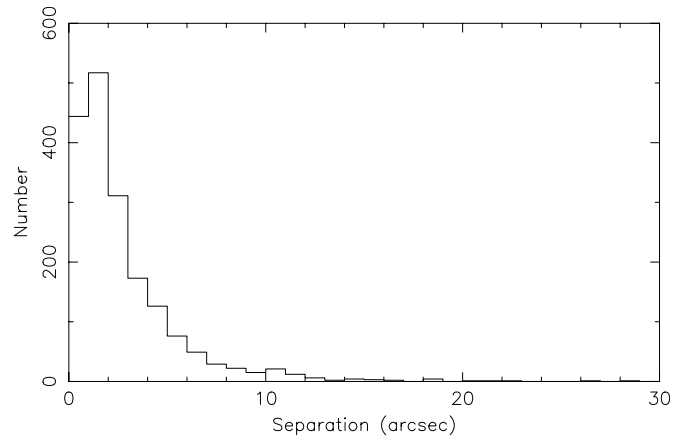

Figure 4. Distribution of the offsets between the catalog *MSX* position and that derived from data with higher spatial resolution.

Currently in the online database, 2781 objects have had their astrometry refined, 1104 using GLIMPSE or other *Spitzer* IRAC data, 942 using 2MASS data, 116 from UKIDSS or VVV data, 398 using radio positions, and 203 using *WISE* data. The remainder of the objects employed MIPS data; two objects used ground-based, thermal infrared images where no other alternative was suitable and 17 objects that still retained their original *MSX* positions.

Figure 4 shows a histogram of the positional differences between the initial *MSX* position and the final adopted positions for this subset of data. The offsets seen that are greater than 15 arcsec mostly correspond to sources that we have split into two or more counterparts, with the exception of the well known H II region G333.6032–00.2184, where even from the *MSX* image the original position is clearly inaccurate. There are, however, sources of all kinds that have not been split, where the astrometry differs in the range of 10–15 arcsec, including those where the counterpart is highly reliable since it is drawn from the GLIMPSE data. In all such cases, a visual inspection of the available GLIMPSE images reveals a complex background with significant extended emission as well as the presence of point sources. Overall, however, the results show that 80% (99%) of the objects have offset differences less than 4.5 (13) arcsec. We stress, however, that the final astrometry is good to better than an arcsecond in almost all cases since it uses much higher spatial resolution data.

The final catalog of potential candidates was only drawn up after this astrometric identification of individual counterparts was completed. Inevitably, this fact meant that we had partial "working versions" of the catalog along the way, which wrongly excluded some objects, generally on the grounds of their having appeared extended in *MSX* images alone (whereas higher resolution data suggested a more point-like source). These objects tend to lack the same depth of coverage in the follow-up observations outlined in Section 2.6, but have been added back into the final catalog with an appropriate classification.

2.5. The Pilot Survey and Final Color Selection Criteria

Our initial multi-color selection criteria for picking massive protostars from the *MSX* catalog was published in Lumsden et al. (2002). That paper relied on object classifications available in the literature. This procedure could have led to a bias, since few of the literature classifications were the results of systematic surveys. In order to determine the reliability of

our source selection using the *MSX* and 2MASS catalogs, we therefore initially carried out a small pilot survey of about 100 sources, all of which lay in the outer Galaxy in order to reduce confusion. The objects were selected based on a single color cut of $F_{21}/F_8 > 1.5$, with *MSX* quality flags set at 4 in both bands. We did not impose a flux or luminosity limit, although in practice the quality threshold implies F_{21} greater than about 5 Jy. This selection encompasses the previously published color selection but includes bluer objects and does not rely on matching with a near-infrared counterpart.

We obtained our own near- and mid-infrared imaging data using UKIRT, as well as spectroscopy of a smaller subsample from the same facility. The spectroscopic data will be published separately in Cooper et al. (2013), together with all of the other spectra obtained at UKIRT as part of the main RMS survey, and both mid- and near-infrared images are available on our database. Here, we are only interested in the overview that these data gave on our color selection. Many of the sources within the pilot survey had already been studied in detail, so that we could draw upon literature classifications to aid in this process, with the spectroscopy also informing our final identifications. The full classification procedure that these data helped inform is discussed in detail in Section 2.6.

The net result of this survey therefore is that our initial supposition from Lumsden et al. (2002) that we can use a combination of *MSX* mid-infrared data and suitable near-infrared data was correct. The final near- and mid-infrared color boundaries we adopted at the completion of this survey are the same as those published in Lumsden et al., namely: $F_{21} > 2F_8$, $F_{21} > F_{14}$, $F_{14} > F_8$, $F_8 > 5F_K$, and $F_K > 2F_J$. The depth of the initial 2MASS catalog guarantees that if we do not detect these objects in the K-band then the available upper limit does satisfy the $F_8 > 5F_K$ constraint. Therefore, we include all these non-detections in our final color-selected sample. The same is true for objects detected in the K-band, but where only upper limits on the flux are present in the J-band, since these also satisfy the $F_K > 2F_J$ criterion.

The mid-infrared boundaries essentially just set the constraint that we expect all YSOs to have rising infrared continua in this wavelength range. The main advantage of adding near-infrared data is to help discriminate against objects that have detached dust shells. In that case, the mid-infrared data may look like those of a YSO, since they arise from the warm dust in the shell. However, the near-infrared data generally reveal the central sources with rather bluer colors than any embedded YSO. The online database also contains data and classifications for objects satisfying only the mid-infrared color cuts, but which fail the near-infrared cuts. We have not subsequently studied such objects in detail as many are evolved stars.

2.6. Follow-up Observations and Object Classification

The goal of the RMS survey was to accurately characterize all of the *MSX* point sources that passed the near- and mid-infrared color selection. The basic observational dataset that exists for the majority of these point sources are as follows: higher resolution mid-infrared imaging than available from *MSX* alone (either ground-based 10 μm observations, e.g., Mottram et al. 2007, or publicly available *Spitzer* data as noted previously), higher resolution and deeper near-infrared data than available from 2MASS as noted in Section 2.3, and longer wavelength far-infrared and sub-mm data in order to constrain the spectral energy distribution, all taken from existing public archives (see Mottram et al. 2010, 2011b). Additionally, we
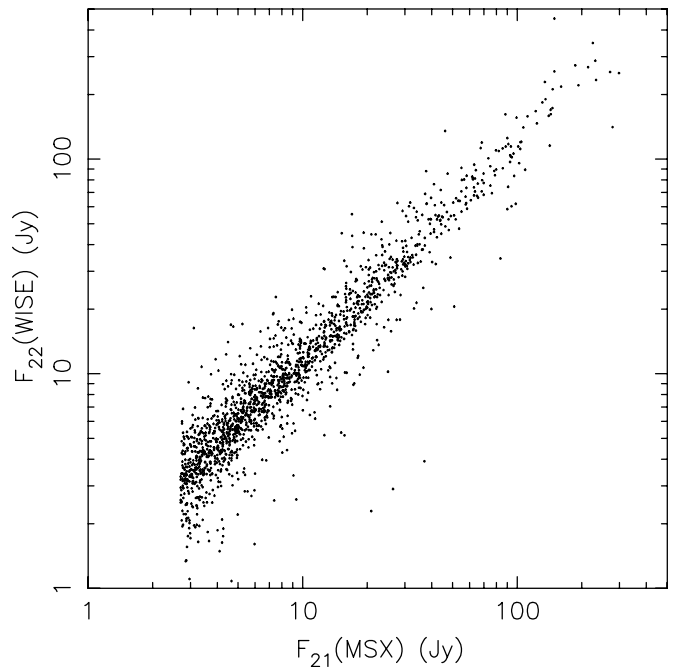
Figure 5. Comparison of the *WISE* 22 μm fluxes for mostly unsaturated sources that can be defined as point-like, with a signal-to-noise ratio > 5, with the 21 μm fluxes for all *MSX* point sources, with quality flag $\geqslant 3$ at 21 μm.

include ^{13}CO $J = 1$–0 or $J = 2$–1 mm line observations in order to determine kinematic distances (Urquhart et al. 2007a, 2008), radio images to study the H II region and PN populations (either our own imaging data—Urquhart et al. 2007b, 2009—or the images present in the CORNISH radio survey—Hoare et al. 2012; Purcell et al. 2013), and, finally, for those objects with appropriate characteristics, $H + K$-band spectroscopy of the identified near-infrared counterpart in the case where that counterpart is sufficiently bright in the K-band (Cooper et al. 2013). In all cases, the published results should always be seen as a snapshot of the contents of the full database at that time. When newer data have become available we have incorporated these into the online version of the catalog, which is the definitive source. The database pools all of this information into a single collection for each source, including images at all wavelengths where we have access to such data. We plan to keep the database updated for the foreseeable future as new information appears.

The final source classification following these observations is decided individually for every source. The full online version of the database contains our reasoning for each source. The basic idea, however, is as follows.

A source that is extended at 8–10 μm with no obvious point-like core is likely to be an H II region or PN, because the dust morphology tends to follow the ionized gas in such regions rather than being concentrated around the central star(s) (e.g., Hoare et al. 1991). YSOs, where the central core is hidden even at 10 μm, can also be slightly extended at the highest resolutions, since we then only see the thermal emission from cavity walls (e.g., de Wit et al. 2010). There is generally a clear distinction between these sources, however.

Any source detected in the radio at a level at $\sim$5 GHz much above 10 mJy must be an H II region or PN (see also Figure 6, which we have used to refine this process). There are examples of known MYSOs with detected radio emission (e.g., Guzmán et al. 2010 found an example from the RMS survey), but all lie below 10 mJy (see also the discussion in Hoare & Franco

Figure 6. Radio luminosity vs. bolometric luminosity for all of the H II regions and YSOs in the catalog (a) showing only the detections and (b) showing all data including limits. The H II regions are crosses and the YSOs are dots (colored red in the online version). Model radio luminosities are also shown in (a) after the fashion outlined in Lumsden et al. (2003). The dot-dashed black line shows the results for a single star using stellar models from Lanz & Hubeny (2007), the dashed line (bl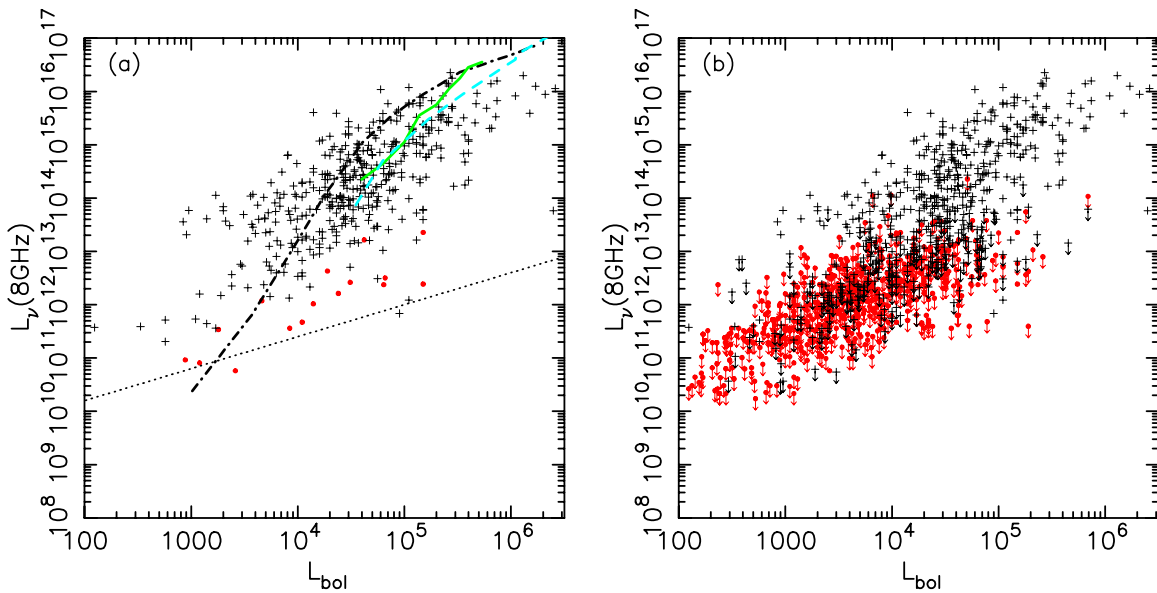ue in online version) shows the results for a single star using stellar models from Pauldrach et al. (2001), and the solid line (green in online version) shows the Pauldrach et al. models but for a cluster. The dotted line shows the extrapolation of jet luminosity as derived for low mass stars by Anglada (1995), as well as of the known emission from high mass stars (whether jet or wind), as given in Hoare & Franco (2007).

(A color version of this figure is available in the online journal.)

2007). These cases illustrate that it is important to be careful when using this criterion alone for weak radio sources. These sources need to be considered according to the expected radio flux as a function of luminosity, as shown in Figure 6.

We classed any source as stellar that has a point-like mid-infrared core (including those sources with diffuse emission around a point-like core), unless the object had significant radio emission. Objects with strong radio emission are likely to be ultracompact H II regions (or very young PNs) if they exceed the flux limit noted above.

The previous criteria serve to identify extended H II regions and PNs, and radio bright point-like H II regions and PNs. The remaining sources were all point-like, and are likely to be either YSOs or evolved stars. Some may be very compact PNs or H II regions, but only if they fall below our radio detection threshold ($\sim$1 mJy in most cases)—Figure 6 shows we are only seriously incomplete in the radio regime below about $L_{bol} \sim 10^4 L_\odot$ (most of the non-detections above this luminosity are objects that are over-resolved by our radio surveys).

Objects that have unambiguous far-infrared counterparts (whether from *IRAS* or MIPSGAL) that reveal a peak in their spectral energy distribution at 25 μm are likely to be evolved. This fact is due to the presence of detached dust shells around most such sources. This class includes most known PNs and all but the most embedded evolved stars.

Any source that is undetected in ^{13}CO $J = 1-0$ is highly likely to be evolved since molecular gas is commonplace in star formation regions. The converse, that no evolved source shows CO emission, is not true, however. Where we have CO emission, we derived kinematic distances in the fashion described in, e.g., Urquhart et al. (2008), using the rotation curve from Reid et al. (2009). For sources within the solar circle, the kinematic distance ambiguity also has to be solved. A discussion of this subject can be found in Urquhart et al. (2012), and we note that we also adopted solutions from Green & McClure-Griffiths

(2011), where their methanol maser sources lie in the same fields and with the same V_{LSR} as our RMS sources. We derived luminosities from the spectral energy distributions (Mottram et al. 2011b) using these derived distances.

Young massive stars generally form in clusters. They also tend to show evidence for reflection nebulosity, outflows, dust lanes, and other features typical of star formation regions. These features are rarer for the main types of evolved stars that we are sensitive to. Therefore, if a source shows extended emission or clustering in either the near- or mid-infrared, it is likely to be young; if it does not, it is likely to be evolved.

We also use our near-infrared spectroscopy in determining the final class. For example, there are some sources that reveal an isolated stellar point source in the near-infrared, but with considerable nebulosity in the field. Spectra obtained of a small sample of these sources reveal about an equal split between evolved stars (presumably seen through an obscuring veil that fills the field) and young stars. The remaining objects in this sub-group for which we have not yet acquired spectra are listed in the catalog as young/old sources.

PNs and H II regions can both also be point-like and below our radio limit, as noted above. Most such sources have near-infrared spectra. Ionized gas emitting under standard Case B recombination leads to a higher equivalent width of the Brγ line of hydrogen (Cooper et al. 2013), allowing a relatively clear discrimination from the generally weaker Brγ seen in YSOs.

Another criterion that can be used to distinguish young and old sources is the presence of maser emission. Methanol masers are characteristic of young massive stars (e.g., Green et al. 2009). The presence of double-peaked OH maser emission is the characteristic classification technique for OH/IR stars (e.g., Eder et al. 1988), while single-peaked or more irregular line profiles can arise in star formation regions.

At the end of this process, we weigh all these factors and decide on a final class. For most objects, this process

is relatively unambiguous. Some, however, have classes that remain uncertain (especially those where we lack portions of the follow-up data).

The final catalog lists 11 categories of objects classified on the basis of these criteria. These comprise five evolved star groups (generic evolved stars, PNs, proto-planetary nebulae, OH/IR stars, and carbon stars), four that are demonstrably young (YSOs, H ɪɪ regions, objects that appear to have characteristics of both of these that we classify as H ɪɪ/YSO, and diffuse H ɪɪ regions), the young/old sources mentioned above, and finally a group of 77 objects that are classified as other (another generic catch-all for objects of known type that do not fall into any other category).

Some of these categories are not necessarily complete. For example, we list known carbon stars separately. Many of the objects we list as evolved stars may also be carbon stars, but we lack the data to discern this fact. Therefore, the complete list of all carbon stars in our sample will contain those classified as such together with some subset of the larger group classified simply as evolved stars. The same is true for OH/IR stars. We have focused much more on the young stars, where our classification is rather more rigorous.

The final classifications were used in producing the color–color diagrams shown in Figure 2. For clarity, we have only plotted objects where data exist to form both colors. There are obviously also many objects with only upper limits at J, K and even 8 μm that are not shown here. We have also plotted only four broad classes of objects on these diagrams. The evolved stars include only the "catch-all" evolved star class in the catalog, plus the carbon and OH/IR stars. There is a clear sense that the majority of the evolved stars defined in this way tend to be rather blue in the thermal infrared. There are a smaller set of genuinely highly reddened evolved stars that do not follow the standard OH/IR or carbon star tracks in Figure 2 (cf. the discussion in Lumsden et al. 2002). The nature of these evolved stars is not clear, although this group appears to exclude all the known carbon stars. A few known OH/IR stars do lie within this genuinely red population.

The other three classes of objects shown are those H ɪɪ regions that are compact enough to be "unresolved" by MSX, PNs (all detected PNs are relatively compact), and all YSOs, regardless of luminosity. The near- and mid-infrared colors do a remarkably good job of separating the PNs from the H ɪɪ regions, consistent with the picture outlined previously that PNs illuminate optically thin dust shells whereas young H ɪɪ regions all live in optically thick environments. Finally, the YSOs fill most of the color space. This result clearly demonstrates the value of detailed follow-up observations, since it would be impossible to color-select our YSO population otherwise without significant contamination by evolved stars, PNs, and H ɪɪ regions. Our spectroscopy of the MYSOs suggests that this wide color dispersion is probably an evolutionary effect, in the sense that the MYSOs become bluer and the dust disperses as they age (Cooper et al. 2013).

2.7. Completeness

In Lumsden et al. (2002), we estimated that we could detect a B0 star anywhere in the Galaxy based on the sensitivity of the original MSX PSC. In Davies et al. (2011), we refined these estimates by determining whether we could recover false sources injected into MSX images, and hence defined a completeness as a function of position in the Galaxy. Here, we consider again whether those estimates were correct by comparing the original MSX data with those from the much more recent $WISE$ mission and also by comparing our final catalog with other published samples of MYSOs or ultra-compact H ɪɪ (UCHII) regions.

The $WISE$ data have better spatial resolution at 10 μm than do the MSX data by a factor of three and they are considerably deeper in limiting flux. $WISE$ does have a relatively faint saturation limit, however, and the published catalog is not a complete $source$ catalog so much as a flux-detection catalog. We first compared the 21 μm fluxes from MSX for all our good sources with the 22 μm sources found in $WISE$. We only considered sources with MSX quality flags of 3 or 4 at 21 μm and limited the $WISE$ counterparts to those that have less than 25% saturated pixels, are relatively point-like (see below), and have a signal-to-noise ratio >5 in the 22 μm band. Figure 5 shows the result for 1658 matched sources. There is clearly a good correlation, with a fair degree of scatter due mostly to extended sources. This result suggests the MSX data are indeed a good basis for our catalog.

We can also use the $WISE$ data to derive a "RMS-like" sample with the same l and b boundaries to test the completeness of our catalog. We used data with a signal-to-noise ratio of at least 5 in all bands, since $WISE$ is much more sensitive than MSX. We further restricted ourselves to compact sources by requiring the χ^2 profile fitting values from the $WISE$ catalog to be less than 15. Figure 5 suggests we restrict ourselves to $F_{22} > 2.8$ Jy for a fair comparison. Finally, equivalent color cuts for our RMS sources are approximately $F_{22} > 2F_{12}$, $F_{22} > 2F_{4.6}$, $F_{4.6} > 1.3F_{3.4}$, and $F_{22} > 10F_K$.

There were 228 objects satisfying these criteria that were not in our RMS catalog. Of these, 156 objects had MSX data. On inspection, all but 10% of these objects are genuine point sources. Of those with counterparts, 97 have MSX $F_{21} < 2.7$ Jy, excluding them from our RMS selection, 24 were in the MSX Singleton (i.e., single detection) list that we did not use, and 101 had MSX colors that fail our color selection (generally inverted F_{14}/F_8 or F_{14}/F_{22} ratios). Objects such as these, which are marginally outside our initial MSX selection criteria, are unlikely to affect our conclusions. For example, if we consider just the flux limit alone, a similar number of sources have been included in our sample that are in reality fainter than our stated flux limit (as easily seen in Figure 5). Of the remaining 72 $WISE$ objects that are not detected by MSX, a visual inspection reveals that only 13 are definitely real, with another 7 possibly so. The others are a mixture of extended objects, regions around saturated objects, and a few very confused regions.

One group of $WISE$ detections that we excluded from our RMS catalog are of greater interest. We excluded objects from our original selection that were detected only at 21 μm, as our experience with MSX suggested single band detections, other than in the deeper 8 μm band, were unreliable. There are 27 objects detected only at 21 μm by MSX that also satisfy the $WISE$ color cuts above, however. These objects all form an unusual category, where their F_{22}/F_{12} ratio is larger than other sources in the RMS survey, but their $F_{4.6}/F_{3.4}$ ratio is fairly normal. The 12 μm images suggest these objects all sit in the core of dark clouds, where the silicate absorption feature is dominating the spectral energy distribution.

Overall, therefore, we can say that $WISE$ finds additional sources that at most amount to about 50 objects, or about 2%–3% of our total final red MSX sample. We therefore conclude that our initial completeness estimates are reasonable for the color selection we adopted.

We can also compare our catalog with other published lists of young massive stars. A complete catalog for UCHII regions exists from the recently completed CORNISH blind radio survey (Purcell et al. 2013). A high-reliability compact HII region catalog (Urquhart et al. 2013b) with clear ATLASGAL counterparts (Schuller et al. 2009) has recently been produced. This catalog identified 207 compact and UCHII regions that lie within the union of the boundaries of CORNISH and ATLASGAL. We recover 160 of these in our final list of good RMS sources. An additional 18 have other *MSX* counterparts within 10 arcsec, with 10 with a 21 μm flux below our limit, seven with brighter 8 μm emission than 14 μm emission (suggestive of strong polycyclic aromatic hydrocarbon, PAH, emission commonly seen around HII regions, but excluded from our color selection), and one only detected by *MSX* at 21 μm (which, as noted above, we excluded from consideration for the RMS catalog). Notably, many of these 18 sources also have stronger emission at 12 μm than at either 8 μm or 14 μm, indicative of strong 12.8 μm [Ne II] emission from their nebulae. Sources such as these are often extended in *MSX*, and would have been classified by us as diffuse HII regions. Inspection of the *Spitzer* GLIMPSE and MIPSGAL images for the sources that have no *MSX* counterparts reveal an equal combination of extended sources that would have also been classified by us as diffuse HII regions and faint sources in complex backgrounds. Overall, we conclude that the use of our color constraints misses about 10% of the total HII region population within our size limits. We used the modeling of Davies et al. (2011) to estimate the fraction missing due to the size constraint itself. Fewer than 5% of UCHII regions are missing anywhere in the Galaxy, consistent with our comparison with the CORNISH catalog. The larger compact HII regions are less well represented, with more than 50% missing, although presumably some fraction of these in reality make up our diffuse HII region category. Therefore, our overall size constraint is strictly only useful in terms of detecting UCHII regions.

We can also compare with the earlier, *IRAS*-based, Chan et al. (1996) and Sridharan et al. (2002) catalogs of high-mass protostellar candidates. For the Chan et al. catalog, if we excluded those outside our survey area, only 14 sources out of 215 are not present in our catalog. We examined these sources in detail. All but one are either in fields where the *IRAS* position falls between two well separated regions of star formation (which are in our catalog), or are genuine objects detected in *MSX* where $F_8 > F_{14}$. Such sources also appear to be multiple HII regions, but largely unresolved by *MSX*. The colors are a reflection of the properties of the individual sources. Virtually none are point sources at the resolution of *WISE* or *Spitzer*. The exception to this fact is IRAS 18079–1756, which has no counterpart in the *MSX* data.

The Sridharan et al. catalog should be a "cleaner" sample of MYSOs, given the greater constraints they place on object selection. In particular, they specifically select against objects with known radio emission in single dish surveys. We find a match for 40 of the 69 sources within 20 arcsec. Examination of the remaining 29 sources shows that 21 have *MSX* counterparts within the same radius. The overwhelming majority of these *MSX* counterparts have inverted spectra, consistent with strong PAH and [Ne II] emission affecting the flux at 8 μm and 12 μm. The same sources also appear significantly extended in the *WISE* images. Overall, these sources appear to be classical extended HII regions, i.e., exactly the sources that Sridharan et al. tried to select *against*. Indeed, many show evidence of radio emission as

well (from CORNISH but also MAGPIS—specifically Helfand et al. 2006). The remaining eight sources appear to have very large scale diffuse emission at 22 μm, with multiple possible exciting sources contained within. We would classify all but four objects as diffuse HII regions. Only one source, IRAS 05553+1631, is a genuine compact source not present in the *MSX* catalog. Again, within our stated selection criteria, there is relatively little evidence of large scale incompleteness in our results for compact infrared bright sources.

Another possible comparison, which may better target the YSO population, is provided by the Methanol Multibeam Survey (MMB; Green et al. 2009). Methanol masers are known to appear only in regions of high mass star formation. The entirety of the southern portion of the MMB survey is now published (see Green et al. 2012). Only 202 of the 554 methanol maser sources that lie within $187° < l < 350°$ appear in our initial RMS candidate list (with a search radius of 20 arcsec). Using a tighter 4 arcsec radius, and considering only matches with our compact sources (i.e., not the diffuse HII regions), reduces this total to 141, of which 93 are YSOs and 48 are HII regions. However, MMB fails to detect emission from 348 of our YSOs, and 506 of our HII regions, within the current published MMB region. Clearly, MMB alone is not a sufficient means of detecting all massive young stars.

In order to determine whether the *MSX* "dark" MMB sources are truly missing, we also looked for them in the *WISE* catalog. This technique recovers 529 of the 554 MMB sources with the same 20 arcsec search radius. Approximately half of these have $F_{22} < 2.7$ Jy. The tighter 4 arcsec search radius reduces this overlap to 355 of 554. These values are consistent with the finding of Gallaway et al. (2013), who did a similar analysis using the GLIMPSE point source catalog. Gallaway et al. also show that the MMB sources without counterparts in our catalog are on average fainter at 8 μm, consistent with our findings here (they also find they are often bluer than our RMS selection criteria). The luminosity distribution of the matches with RMS is also informative in this analysis, since it shows that 43 of the 141 sources have $L \leqslant 10^4\,L_\odot$. The objects that are genuinely "dark" are clearly of interest, since they may represent a heavily embedded phase that we are not fully sensitive to, but these only comprise about 10% of the MMB population (Gallaway et al). The others are consistent with a population of lower luminosity sources, or much more distant sources with luminosity $\sim 10^4\,L_\odot$ (i.e., just below our completeness limit). Urquhart et al. (2013a) present a more detailed analysis of the counterparts of these maser sources. Their findings are consistent with the simple analysis presented here.

Overall, therefore, the evidence suggests that the RMS survey is greater than 95% complete within its color and flux cuts. This fact is true regardless of which alternative survey we compare the RMS survey against. In addition, we have also quantified the incompleteness due to our actual selection criteria. The main contributor to missing "young" sources comes from unusual colors and from the failure to recover very red sources. We conclude that the RMS survey recovers greater than 90% of all compact young massive sources with mid-infrared emission.

3. THE CATALOG

The RMS catalog is continuously being updated as new information becomes available. In particular, we are still refining distances when new information appears. The current catalog uses the Reid et al. (2009) model that accounts for the known

Table 1
The Full RMS Catalog

RMS Name	R.A.	Decl.	Type	Color Cut?	v_{LSR} (km s^{-1})	Near (kpc)	Far (kpc)	Adopted (kpc)	R_{gc} (kpc)	L_{bol} ($L_\odot$)	IRAS
G010.0997+00.7396	18:05:13.10	−19:50:34.7	PN	N							
G010.1089+00.3716	18:06:36.30	−20:00:51.4	PN	Y							18036-2001
G010.1481-00.4260	18:09:39.55	−20:21:59.6	Evolved star	N							
G010.3204-00.2616	18:09:23.29	−20:08:06.9	H II region	Y	32.1	3.8	12.8				18064-2008
G010.3207-00.2329	18:09:17.25	−20:07:18.2	H II region	N	32.5	3.8	12.8				
G010.3208-00.1570A	18:09:00.36	−20:05:08.6	H II region	Y	12.0	2.0	14.6	3.5	4.95	84500	
G010.3208-00.1570B	18:09:01.48	−20:05:08.0	YSO	Y	12.0	2.0	14.6	3.5	4.95	41620	
G010.3844+02.2128	18:00:22.67	−18:52:09.7	YSO	Y	5.5	1.1	15.5	1.1	7.35	1180	17574-1851
G010.3930+00.5389	18:06:34.27	−19:41:05.3	PN	Y							18036-1941
G010.4413+00.0101	18:08:37.94	−19:53:59.0	H II region	Y	66.4	5.3	11.2	11.2	3.3	40020	18056-1954

(This table is available in its entirety in a machine-readable form in the online journal. A portion is shown here for guidance regarding its form and content.)

parallax distances (e.g., Rygl et al. 2010). Where individual sources have themselves been studied using maser parallaxes, we also adopt the parallax distance. The initial kinematical information is all provided in the database to allow users to adopt the Galactic rotation model of their choice.

In addition, we are extending the wavelength coverage of the spectral energy distribution and adding data with better spatial resolution when it becomes available. The online database includes images of our fields as well as spectra, all downloadable as FITS files. In addition, a search function makes it possible to query the catalog directly, allowing users to select subsamples appropriate to their studies. We are always interested in adding functionality that will make the RMS database more useful and we welcome suggestions for extensions. The only definitive version of the catalog is therefore online, at http://rms.leeds.ac.uk/.

The version presented here provides a subset of the catalog information. Table 1 lists the RMS name, position, source type, a flag indicating whether the source passed the near-infrared color cuts (all sources by definition pass the *MSX* cuts), v_{LSR}, kinematic near and far distance, adopted distance (which, if different, indicates a non-kinematic origin for the distance such as parallax), Galactocentric radius, luminosity, and *IRAS* counterpart, if one exists. The color cut is defined by identifying *blue* objects with the simple prescription $F_K/F_J < (2 - \delta(F_K/F_J)$ or $F_8/F_K < (5 - \delta(F_8/F_K)$, where δ represents the errors in the derived ratio. These represent objects that must be too blue to fall in our sample. We use the best near-infrared data available for each source in calculating these ratios.

Table 2 presents the subset of massive protostars that pass all color cuts, and additionally have $L_{\mathrm{bol}} > 20000\,L_\odot$. This table gives position, adopted distance, luminosity, and commonly used "Other Name." These names are only given for sources with more than 10 citations on SIMBAD for counterparts within 20 arcsec of the central RMS source. We present all the objects we classify purely as YSOs, as well as those that have clear characteristics of H II regions (e.g., strong radio emission), but where the central exciting star still retains characteristics of a YSO, such as spectral evidence for a disk (see, e.g., Cooper et al. 2013). Only about half of our most luminous protostars are sufficiently well studied to have a common "Other Name." This result clearly illustrates the additional benefits provided by the RMS survey for the study of luminous protostars.

4. THE PROPERTIES OF YOUNG MASSIVE STARS

More detailed analysis of some of the bulk properties have already been presented in our other papers. For example, we have modeled the young massive star population of the Galaxy and our observational data then rule out models in which the accretion rate decreases with time (Davies et al. 2011). We also find a maximum luminosity for an MYSO of about $2 \times 10^5\,L_\odot$ that is consistent with the Davies et al. and Hosokawa et al. (2010) models (Mottram et al. 2011a). We can derive lifetimes and luminosity functions for both the MYSO and compact H II region phases (Mottram et al. 2011a). We have also mapped the distribution of the young massive star population in the Galaxy and shown how well it correlates with spiral arm structure (Urquhart et al. 2011a).

Here, we consider some of the properties that the catalog as a whole reveals about the young massive stellar population of the Milky Way that utilize the breadth of the data from our follow-up observations.

4.1. The Anomalous Radio Luminosity of Young B Stars

In Figure 6, we show the radio versus bolometric luminosity. A clear envelope to the detected H II region emission can be seen in the figure, which must represent the maximum optically thin free-free emission. We can compare these results with the predictions from OB stellar atmosphere models. We have plotted three model sequences here. The first two use the WM-basic models of Pauldrach et al. (2001), in the fashion outlined in Lumsden et al. (2003), for a single central exciting star and for a cluster of such stars following a standard initial mass function. The last model sequence uses the same data as applied in the modeling of Davies et al. (2011), with the stellar models coming from Martins et al. (2005) and Lanz & Hubeny (2007). In all cases, we convert the model N_{LyC}, the number of Lyman continuum photons, to a radio flux using Equation (4) from Kurtz et al. (1994):

$$S_\nu(\mathrm{Jy}) = 1.32 \times 10^{-49} \epsilon a N_{\mathrm{LyC}}$$
$$\times \left(\frac{\nu}{\mathrm{GHz}}\right)^{-0.1} \left(\frac{T_e}{\mathrm{K}}\right)^{0.5} \left(\frac{d}{\mathrm{kpc}}\right)^{-2}, \quad (1)$$

where $\epsilon = 1$ is the fraction of the Lyman continuum ionizing flux that actually ionizes the gas (as opposed to exciting dust, or simply leaking away), $a \sim 0.98$, and we adopt an electron temperature $T_e = 8000$ K.

Table 2
Complete List of Massive Protostars with $L > 20{,}000\,L_\odot$

Name	R.A.	Decl.	D (kpc)	L_{bol} ($L_\odot$)	Other Name	Name	R.A.	Decl.	D (kpc)	L_{bol} ($L_\odot$)	Other Name
G010.3208-00.1570B	18:09:01.48	−20:05:08.0	3.5	41,600		G010.8411-02.5919	18:19:12.10	−20:47:30.9	1.9	23,700	GGD 27
G012.0260-00.0317	18:12:01.89	−18:31:55.8	11.1	24,600	IRAS 18090-1832	G012.1993-00.0342B	18:12:23.43	−18:22:51.0	12.0	34,700	IRAS 18094-1823
G012.9090-00.2607	18:14:39.56	−17:52:02.3	2.4	21,700	W33A	G017.6380+00.1566	18:22:26.38	−13:30:12.0	2.2	53,100	GL2136
G017.9789+00.2335A	18:22:49.14	−13:10:01.5	14.4	31,300		G018.3412+01.7681	18:17:58.11	−12:07:24.8	2.8	21,800	IRAS 18151-1208
G020.7617-00.0638B	18:29:12.11	−10:50:36.2	11.8	20,800		G021.5624-00.0329	18:30:36.07	−10:07:11.1	9.7	23,700	
G023.3891+00.1851	18:33:14.32	−08:23:57.5	4.5	41,900		G026.2020+00.2262	18:38:18.51	−05:52:57.5	7.5	30,500	
G027.1852-00.0812A	18:41:13.18	−05:09:01.0	13.0	94,300	IRAS 18385-0512	G028.3046-00.3871A	18:44:21.97	−04:17:39.5	10.0	38,500	
G028.8621+00.0657	18:43:46.25	−03:35:29.3	7.4	146,200	IRAS 18411-0338	G029.8620-00.0444	18:45:59.55	−02:45:06.5	7.3	56,000	CH3OH 029.86-00.05
G030.1981-00.1691	18:47:03.07	−02:30:36.1	7.3	33,200		G030.9585+00.0862B	18:47:31.83	−01:42:59.6	11.7	50,400	
G030.9727+00.5620	18:45:51.69	−01:29:13.0	12.6	22,900		G032.0451+00.0589	18:49:36.56	−00:45:45.5	4.9	20,400	IRAS 18470-0049
G032.9957+00.0415A	18:51:24.45	+00:04:34.1	9.2	22,500	IRAS 18488+0000	G034.0126-00.2832	18:54:25.06	+00:49:56.6	12.9	33,800	
G034.0500-00.2977	18:54:32.30	+00:51:32.9	12.9	22,500		G035.1979-00.7427	18:58:13.00	+01:40:31.2	2.2	30,900	G35.2N
G037.5536+00.2008	18:59:09.95	+04:12:15.7	6.7	38,000	IRAS 18566+0408	G042.0341+00.1905A	19:07:28.20	+08:10:53.3	11.1	29,300	
G042.0977+00.3521A	19:07:00.51	+08:18:44.1	10.9	31,300	IRAS 19045+0813	G042.0977+00.3521B	19:07:00.52	+08:18:45.6	10.9	31,300	IRAS 19045+0813
G042.1099-00.4466*	19:09:53.57	+07:57:14.5	8.7	43,400	IRAS 19074+0752	G043.0884-00.0109	19:10:09.55	+09:01:26.7	11.1	32,900	
G045.4543+00.0600B	19:14:21.27	+11:09:15.5	7.3	34,900	IRAS 19120+1103	G045.4543+00.0600C	19:14:21.24	+11:09:20.2	7.3	34,900	IRAS 19120+1103
G053.6185+00.0376	19:30:23.04	+18:20:26.6	7.9	20,000		G060.5750-00.1861	19:45:52.50	+24:17:42.8	7.5	30,100	IRAS 19437+2410
G060.8828-00.1295B*	19:46:20.14	+24:35:29.3	2.2	21,700	S87 IRS1	G062.5748+02.3875	19:40:21.52	+27:18:43.7	13.4	96,100	IRAS 19383+2711
G064.8131+00.1743	19:54:05.86	+28:07:40.6	8.2	184,300	IRAS 19520+2759	G073.6525+00.1944	20:16:21.96	+35:36:06.3	11.2	259,200	IRAS 20144+3526
G075.6014+01.6394	20:15:48.16	+38:01:31.3	11.2	28,600		G076.3829-00.6210*	20:27:26.77	+37:22:47.8	1.4	39,700	S106 IRS4
G078.7641+01.6862	20:24:51.67	+40:39:25.3	10.5	42,300		G078.8867+00.7087	20:29:24.87	+40:11:19.4	3.3	185,300	GL2591
G085.4102+00.0032A	20:54:14.36	+44:54:04.6	5.5	20,400		G090.2095+02.0405	21:03:41.76	+49:51:47.1	7.4	29,700	IRAS 21020+4939
G094.4637-00.8043	21:35:09.11	+50:53:09.6	4.9	20,800	IRAS 21334+5039	G094.6028-01.7966	21:39:58.25	+50:14:20.9	4.9	43,200	V645 Cyg
G096.5438+01.3592	21:35:43.82	+53:53:09.4	7.0	22,600	IRAS 21340+5339	G097.5268+03.1837B	21:32:11.30	+55:53:39.9	6.9	30,600	
G097.5268+03.1837C	21:32:10.69	+55:53:35.4	6.9	21,700	S128 IRS 2	G102.3533+03.6360	21:57:25.19	+59:21:56.7	8.4	107,000	CPM 36
G110.1082+00.0473B*	23:05:10.15	+60:14:42.8	4.3	28,400	S156A	G111.2348-01.2385	23:17:21.02	+59:28:48.0	4.4	41,900	IRAS 23151+5912
G111.2824-00.6639B	23:16:03.85	+60:01:56.8	3.5	24,700	IRAS 23138+5945	G111.5671+00.7517	23:14:01.76	+61:27:19.9	2.7	44,600	NGC 7538 IRS 9
G133.6945+01.2166A	02:25:30.99	+62:06:21.0	2.0	28,500	W3 IRS4 (part)	G133.7150+01.2155	02:25:40.78	+62:05:52.5	2.0	206,300	W3 IRS5
G135.2774+02.7981	02:43:28.65	+62:57:08.7	6.0	28,500	IRAS 02395+6244	G151.6120-00.4575	04:10:11.86	+50:59:54.5	6.4	21,500	CPM 12
G192.6005-00.0479	06:12:54.01	+17:59:23.1	2.0	35,600	S255 IRS1	G196.4542-01.6777	06:14:37.06	+13:49:36.5	5.3	94,000	IRAS 06117+1350
G269.8539-00.0630	09:11:08.34	−48:15:56.3	8.4	27,600		G274.0649-01.1460A	09:24:42.55	−52:01:50.6	5.7	24,300	
G281.0472-01.5432	09:59:15.88	−56:54:39.3	7.0	145,100		G281.7578-02.0132	10:01:21.58	−57:42:56.4	7.0	32,300	
G282.0598-00.5721	10:09:26.56	−56:43:49.5	4.9	20,000		G282.8969-01.2727	10:11:31.60	−57:47:03.7	7.0	31,900	
G289.9446-00.8909A	11:01:10.67	−60:57:08.4	8.3	26,200							
G299.5265+00.1478	12:21:50.64	−62:31:42.4	7.5	34,700							
G300.5047-00.1745A	12:30:03.60	−62:56:48.4	8.9	42,700		G301.8147+00.7808A	12:41:53.87	−62:04:14.6	4.4	22,000	IRAS 12389-6147
G303.9973+00.2800*	13:00:41.62	−62:34:20.8	11.4	20,400		G304.3674-00.3359A	13:04:09.87	−63:10:20.1	11.8	88,200	
G304.6668+00.9654*	13:07:08.37	−63:47:02.8	11.4	24,800		G305.2017+00.2072A	13:11:10.45	−62:34:38.6	4.0	30,300	CH3OH 305.20+00.21
G305.3676+00.2095	13:12:36.49	−62:33:32.3	4.0	28,100		G305.5610+00.0124	13:14:26.37	−62:44:30.5	4.0	42,000	
G308.9176+00.1231A	13:43:01.70	−62:08:51.2	5.3	186,800	OH 308.918+00.123	G309.9206+00.4790B	13:50:42.34	−61:35:07.9	5.4	26,600	IRAS 13471-6120
G310.0135+00.3892	13:51:37.86	−61:39:07.5	3.2	54,600	IRAS 13481-6124	G319.3993-00.0135C	15:03:17.68	−58:36:14.8	11.7	109,800	
G319.8366-00.1963	15:06:54.49	−58:32:58.8	11.7	38,900		G321.0523-00.5070	15:16:06.11	−58:11:41.8	9.1	74,400	
G321.3824-00.2861	15:17:20.21	−57:50:00.3	9.4	24,600		G327.1192+00.5103	15:47:32.81	−53:52:39.4	4.9	41,600	CH3OH 327.120+00.511
G328.2523-00.5320A	15:57:59.83	−53:58:00.5	2.9	40,500	CH3OH 328.25-00.53	G328.2523-00.5320B	15:57:59.38	−53:57:57.4	2.9	21,300	
G329.0663-00.3081	16:01:09.93	−53:16:02.3	11.6	65,600	CH3OH 329.07-00.31	G331.2759-00.1891B	16:11:26.00	−51:41:57.0	4.9	35,000	CH3OH 331.278-00.188

Table 2
(Continued)

Name	R.A.	Decl.	D (kpc)	L_{bol} ($L_\odot$)	Other Name	Name	R.A.	Decl.	D (kpc)	L_{bol} ($L_\odot$)	Other Name
G331.3576+01.0626	16:06:25.78	−50:43:22.0	4.5	22,200	IRAS 16026-5035	G331.5131-00.1020	16:12:09.96	−51:28:37.1	5.0	69,300	OH 331.512-00.103
G331.5180-00.0947A	16:12:08.95	−51:28:02.3	5.0	32,100		G331.7953-00.0979	16:13:28.04	−51:16:46.8	14.5	105,300	
G332.0939-00.4206	16:16:16.47	−51:18:25.2	3.6	76,100		G332.8256-00.5498A*	16:20:11.07	−50:53:16.2	3.6	207,700	
G332.9868-00.4871	16:20:37.81	−50:43:49.7	3.6	26,700		G333.1256-00.4367	16:21:02.66	−50:35:55.4	3.6	85,000	CH3OH 333.126-00.440
G334.8438+00.2095A	16:25:40.51	−48:55:16.2	10.6	25,400		G336.8308-00.3752	16:36:26.16	−47:52:30.9	13.5	50,900	
G338.0008-00.1498A	16:40:04.02	−46:51:18.1	11.4	50,400		G338.2253-00.5094	16:42:30.98	−46:55:22.6	13.7	103,000	
G338.3597+00.1430A	16:40:11.88	−46:23:27.2	12.8	30,100		G338.4712+00.2871	16:39:58.91	−46:12:36.5	13.1	86,100	IRAS 16363-4606
G338.4763+00.0418A	16:41:04.46	−46:22:18.8	12.6	28,200		G338.9196+00.5495	16:40:34.05	−45:42:08.0	4.2	32,000	
G339.3316+00.0964	16:44:04.39	−45:41:27.2	13.1	39,600		G339.6221-00.1209	16:46:06.00	−45:36:43.9	2.8	23,800	
G339.8838-01.2588	16:52:04.66	−46:08:33.6	2.7	63,900	IRAS 16484-4603	G339.9489-00.5401	16:49:07.95	−45:37:58.8	10.5	20,800	EGO G339.95-0.54
G342.9583-00.3180	16:58:48.56	−43:09:32.5	12.7	62,200		G343.1261-00.0623	16:58:17.21	−42:52:07.1	2.8	66,100	IRAS 16547-4247
G344.4257+00.0451C	17:02:08.62	−41:47:10.2	4.7	23,100		G344.6608+00.3401	17:01:41.02	−41:24:48.1	12.7	20,300	
G345.4938+01.4677	16:59:41.61	−40:03:43.4	2.4	154,400	IRAS 16562-3959	G345.5043+00.3480	17:04:22.87	−40:44:23.5	2.0	23,700	CH3OH 345.50+00.35
G349.7215+00.1203A	17:18:11.22	−37:28:24.6	11.3	65,900							

Note. Objects marked with a superscript ∗ are also the central stars of H II regions.
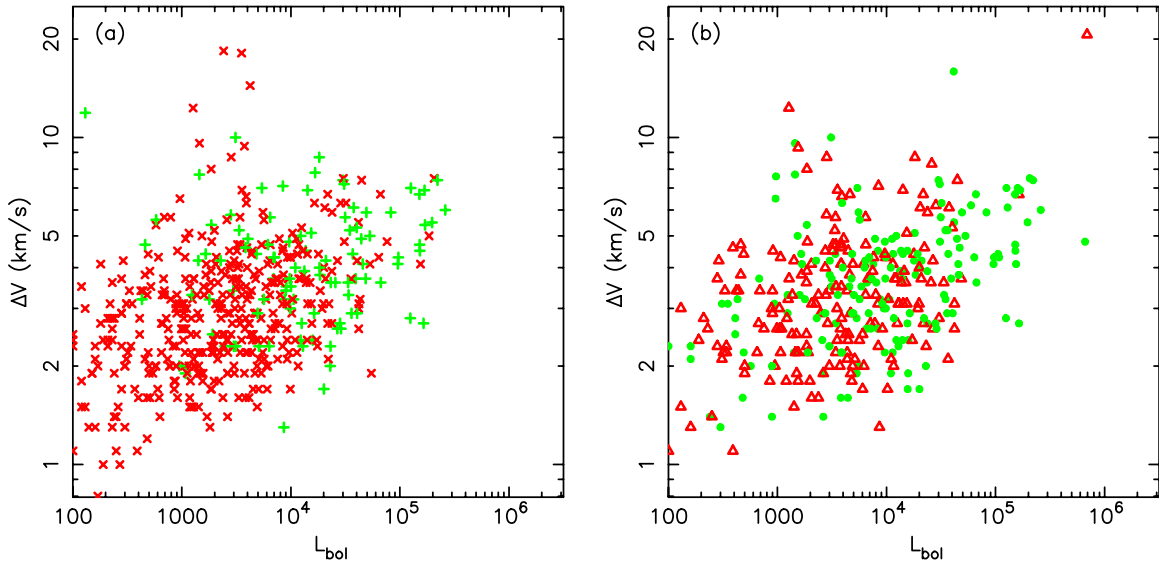
Figure 7. Linewidth vs. bolometric luminosity of our observed ^{13}CO data. The sample is limited to those objects with distances less than 5 kpc for comparison with the results of Figure 9. The data for YSOs ($\times$s; colored red in the online version) and H II regions ($+$s; colored green in the online version) are shown in (a) and the same set of data but split by color are shown in (b), with the points (green in the online version) having $F_{21}/F_8 > 10$ and the triangles (red in the online version) having $4 < F_{21}/F_8 < 10$.

(A color version of this figure is available in the online journal.)

The detected H II regions with $L \lesssim 5\times10^4\,L_\odot$ all tend to show more emission than the models. Since this plot shows luminosity versus luminosity, the issue cannot lie wholly with inaccurate distances. Errors in the fluxes used in estimating the bolometric luminosity are likely to move points to the left, if anything, since we still rely in part on large-beam *IRAS* data for objects outside the MIPSGAL region. Objects can be fainter than the envelope, since optical depth, leakage of ionizing photons from the nebula, and over-resolved interferometric data all conspire to produce less flux than expected. Nothing, however, acts to make an object brighter in the radio than anticipated. The fact that the envelope is so well defined, even at low luminosity, strongly suggests this is a real effect.

Significant excess Lyman continuum flux above model predictions has been observed directly in EUV observations of the nearby stars ϵ and β CMa (Cassinelli et al. 1995, 1996). These are B2 II and B1 II–III spectral types and hence are not on the main sequence and thus perhaps not direct analogs of the young B stars ionizing UCHII regions. However, if these young stars have not completely contracted onto the main sequence, they may not be so dissimilar. The timescales for the contraction onto the main sequence, after the termination of accretion are of order 10^5 yr for early B stars (Figure 2 in Davies et al. 2011), which is similar to the age of the UCHII regions themselves.

The physical reasons behind the order of magnitude excess Lyman continuum flux are still being sought. An infrared excess in the B2 II stars showed that the outer layers of the atmosphere were warmer than the models predict. Krticka et al. (2005) discuss the effects of Doppler and frictional heating of stellar winds that are significant in the cooler B stars. The hot, X-ray dominated winds in some late O main sequence stars may also be of relevance here (Huenemoerder et al. 2012).

Finally, Figure 6(a) clearly shows that most of the detected MYSOs lie below the H II region detections. The radio emission from these objects is not nebular. The stars simply lack ultraviolet flux (as is also evident from the near-infrared spectra presented by Cooper et al. 2013). They are therefore "radio weak" compared to the H II regions with the same luminosity. This

deficit of ultraviolet photons is in agreement with models for MYSOs that predict that the star swells and cools as it accretes (e.g., Hosokawa & Omukai 2009). Two possible alternatives then exist for the source of the radio emission. We may be seeing emission from an ionized jet (see, e.g., Figure 5 in Anglada 1995, which we have fitted together with the known high mass radio detections in YSOs from Hoare & Franco 2007, to derive a relationship through the luminosity regime in Figure 6). This jet perhaps lies at the base of any larger scale molecular outflow. Alternatively, we may be seeing an equatorially flattened wind (e.g., Hoare 2006). The relative paucity of actual detections in our existing radio data, as well as their relatively modest spatial resolution, makes it impossible to distinguish between these cases.

4.2. Virialized Motions in Massive Cores?

As part of the follow-up observations for the RMS survey, we have acquired a significant quantity of new mm CO line data in order to derive kinematic distances to our sources. The line intensities were not fully calibrated, but the velocities and line widths are.

In Figure 7, we plot the relationship for H II regions and YSOs between the full width at half maximum of the ^{13}CO emission and the bolometric luminosity. We have curtailed the sample to those with distances within 5 kpc, and limited the H II regions to those objects that appear point-like in the *WISE* data (see Section 2.7 for details). The left-hand plot shows where the H II regions and YSOs lie separately and the right-hand plot shows all H II regions and YSOs but instead shows where objects fall as a function of the F_{21}/F_8 ratio, where we have split the data into two groups at $F_{21}/F_8 = 10$. The more luminous objects in Figure 7 have broader lines. The formal Pearson correlation coefficient between $\log(\Delta v)$ and $\log L$ is $\sim$0.43 for 523 objects. Urquhart et al. (2011b) found a similar relationship using the width of the NH$_3$ line for an overlapping but not identical sample of YSOs and H II regions drawn from the RMS survey.

The correlation holds separately for YSOs, with a correlation coefficient of 0.41 for 422 YSOs. By comparison, the H II region
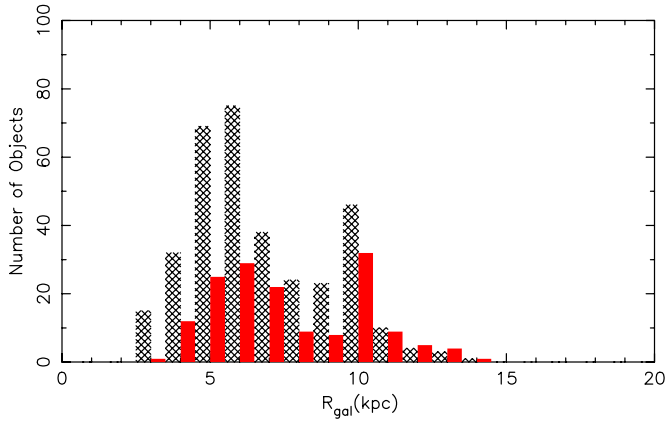
Figure 8. Distribution of Galactocentric radius for H II regions (gray hatched bars) and YSOs (solid, colored red in online version). Only sources with bolometric luminosities greater than $10^4 L_\odot$ and distances less than 10 kpc are included.

(A color version of this figure is available in the online journal.)

sample on its own shows no significant evidence for a correlation (a correlation coefficient of 0.10 for 101 H II regions, rising to 0.19 if the restriction on "point-like" H II regions is removed). It is possible that the bulk expansion motions seen in the gas around H II regions destroys any correlation there. Not all of our YSOs show evidence for an outflow (L. T. Maud et al., in preparation), which suggests that the good correlation seen for the YSOs is actually a fundamental property of the natal molecular cloud rather than due to the energetics of the central source.

Urquhart et al. suggested that this relationship was due to the correlation between linewidth and the mass of the natal clump (i.e., it is essentially a virial relation, e.g., Larson 1981), and that seems to be the most natural explanation here too. Potentially, this explanation also accounts for the weak color segregation present in F_{21}/F_8, since we would expect the objects that will become more massive to have higher accretion rates and hence have redder colors in the thermal infrared. High accretion rates can only be sustained if the core itself is more massive, naturally leading to redder objects having somewhat enhanced linewidths.

4.3. Galactocentric Radial Distribution of RMS Sources

The distribution of the RMS sources in the Galaxy has previously been considered by Urquhart et al. (2011a), but we are now in a position to accurately study how this distribution varies with source type. In Figure 8, we show the distribution of both H II regions and YSOs as a function of Galactocentric radius. We have restricted the sample to those objects with $L_{bol} > 10,000 L_\odot$ and distances less than 10 kpc to match the rough completeness limit of the catalog. A Mann–Whitney U-test suggests that the distributions of galactocentric radius for the MYSOs and H II regions differ in the sense that the YSOs lie at larger radii at the 99% confidence level. This result could partly be a selection effect. It is easier to see bright radio emitting H II regions in the considerable background near the Galactic center than it is a YSO. There is a lack of H II regions in the outer Galaxy compared to the YSOs, however, and this fact cannot be a selection effect. In part, a luminosity effect may also be in play. If we compare the YSOs against the H II regions with $L_{bol} < 100,000 L_\odot$, the confidence level drops to 95%. This value was chosen as the approximate upper limit of YSO luminosity. In contrast, the samples are different at above the

99% confidence level when we compare the higher luminosity H II regions with the YSOs. There is only one H II region with luminosity above this threshold beyond a Galactocentric radius of 10 kpc—the other 62 all lie closer than 10 kpc.

The most obvious explanation if this result is correct is that high mass cores are more likely in the crowded central regions. Lépine et al. (2011) have found a similar "step-change" in numbers of open clusters and the metallicity gradient at a similar Galactocentric distance of 8.5 kpc. These authors explain this result as being due to a gap in the dense gas at the co-rotation radius that isolates properties in the inner Galactic plane from those outside the co-rotation radius. Their explanation requires smaller gas flows outside the co-rotation radius, which will lead to less collisions between cloud cores. It seems plausible that the most massive star formation regions arise through such collisions (e.g., van Loo et al. 2007), giving a natural explanation for the result we see.

4.4. Color–Luminosity Relationships

Finally, we consider how the colors of the YSOs and H II regions vary as a function of luminosity. Figure 9 shows data using the *MSX* F_{21}/F_8 ratio as well as the ratio from *WISE* bands 3 and 2 (12 μm and 4.6 μm). The latter is especially useful since the beam size for these wavelengths is a factor of three smaller than for the *MSX* data. Again, we have curtailed the sample to those sources that appear point-like in *WISE* at 12 μm and lie within 5 kpc. The latter is important here since we see more H II regions at greater distances due to their greater luminosity on average. The line of sight extinction, and hence to some extent the thermal infrared color, increases with distance, creating a bias.

The H II regions, on average, are redder than the YSOs in both ratios. This result points toward a picture in which H II regions are more embedded. The only other factor that can play a part is geometry. Geometry may have an effect in two ways. Orientation is important in determining the colors of a YSO, since a more edge-on accretion disk source will suffer greater extinction than one we see pole-on. However, the data shown should randomly sample all inclinations. This fact may give rise to the large observed scatter in color, but cannot explain the difference between the H II regions and the YSOs. The second factor is the extent of the H II region. More evolved H II regions, as they grow larger, naturally support a greater volume of Lyα-heated dust. This fact should shift the colors blueward, since there is more emission away from the center of the natal core. Again, part of the scatter could be due to this effect. Since this factor should make H II regions bluer, however, it cannot explain why H II regions are actually redder than YSOs. The colors, like the virial estimates, again suggest more massive cores, which have a greater line of sight reddening toward the center of the core, give rise to higher luminosity sources.

5. SUMMARY

The final catalog from the RMS survey presents a comprehensive view of the infrared bright phase of the massive protostellar population of our Galaxy. The catalog is complete for objects as faint as a typical B0 star at the distance of the Galactic center and for more luminous sources across the whole Galaxy. We currently have almost 700 YSOs and H II regions with confirmed luminosities above this threshold. In addition, we have identified many more YSOs that can be characterized as embedded Herbig Be stars that lie below this luminosity, providing a valuable,
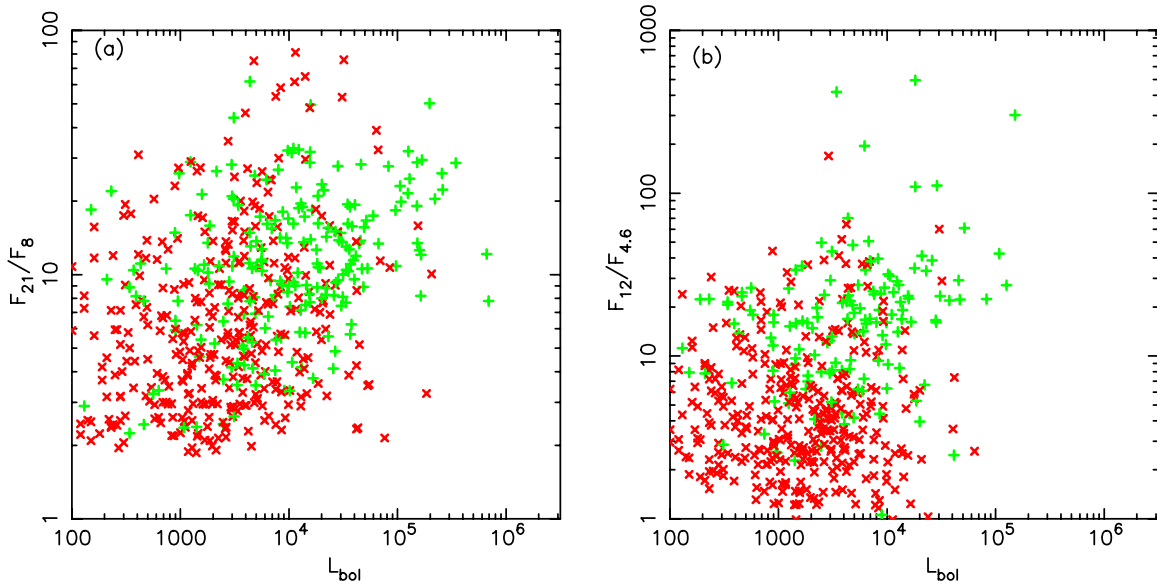
Figure 9. Mid-infrared color vs. bolometric luminosity. The left-hand plot shows data from the *MSX* satellite and the right-hand plot shows data from *WISE*. The sample is limited to those objects with distances less than 5 kpc. The YSOs are shown as ×s (colored red in online version) and H II regions are shown as +s (colored green in online version). There is a clear trend that the H II regions are redder than the YSOs, on average.

(A color version of this figure is available in the online journal.)

although incomplete, resource for the study of young intermediate mass stars as well. The combination of a bright saturation limit for the initial *MSX* catalog, together with the coverage of the whole Galactic plane out to $|b| < 5°$, makes it the ideal catalog for these infrared bright sources. Comparison with both older and lower spatial resolution catalogs of MYSOs derived from *IRAS* and more recent higher spatial resolution candidates from both *Spitzer* and *WISE*, as well as high resolution radio studies, suggests that our catalog is highly reliable and complete for the MYSO class. This catalog is likely to remain the best source for this infrared bright phase for some time, given the relatively low saturation limits of the IRAC and MIPS instruments from *Spitzer* and, to a lesser extent, the detectors on *WISE*. This fact compromises the ability of those missions to study the most massive star formation regions and most luminous sources.

The full RMS catalog has also been used by other groups for aspects of research about massive star formation. Guzmán et al. (2010, 2012) have studied the radio properties of objects they classify as "radio weak," in a bid to detect hypercompact H II regions, jets, and stellar winds. Thompson et al. (2012) examined the incidence of triggering using RMS sources around bubbles found in *Spitzer* data. Moore et al. (2012) studied the correlation of available gas reservoirs with our MYSOs in order to determine how star formation efficiency varies as a function of location within the spiral arms. Davies et al. (2012) used the distances we have derived to YSOs and H II regions to help pin down the distances to massive star clusters. In addition, other groups have adopted similar color selection criteria to those presented in Lumsden et al. (2002) in order to study heavily obscured evolved stars (e.g., Ortiz et al. 2005). Our catalog contains a large number of highly obscured evolved stars likely to be of interest to those studying topics such as post-asymptotic giant branch evolution.

We have also shown that the wealth of data we have acquired can themselves identify both new properties (the excess UV flux from young intermediate mass stars) as well as provide indications as to how massive stars form. The correlation between luminosity and apparent virial mass suggests that

these dynamical processes are essentially responsible for setting the initial conditions rather than the ongoing formation. This result tends to favor models of monolithic collapse, although competitive accretion may play an important role at an earlier phase when the clumps themselves are merging, and possibly also in feeding residual mass to the most massive star present once it has formed. The split between inner and outer Galaxy may also signify the greater role that triggering and spiral density waves can play in denser environments.

Finally, we note that the RMS catalog is already the basis for numerous further studies in massive star formation, such as the properties of outflows. When combined with appropriate catalogs of the initial phases of massive star evolution from other indicators (e.g., Caswell et al. 2010; Contreras et al. 2013; Molinari et al. 2010), a complete census, and an understanding of the evolution of the massive star population from initial core through to main sequence will be possible. These advances should provide firm answers to the remaining questions as to how massive stars form.

REFERENCES

Anglada, G. 1995, RMxAC, 1, 67
Benjamin, R. A., Churchwell, E., Babler, B. L., et al. 2003, PASP, 115, 953
Bonnell, I. A., Vine, S. G., & Bate, M. R. 2004, MNRAS, 349, 735
Campbell, B., Persson, S. E., & Matthews, K. 1989, AJ, 98, 643
Carey, S. J., Noriega-Crespo, A., Mizuno, D. R., et al. 2009, PASP, 121, 76
Carpenter, J. M., Snell, R. L., Schloerb, F. P., & Skrutskie, M. F. 1993, ApJ, 407, 657
Casali, M., Adamson, A., Alves de Oliveira, C., et al. 2007, A&A, 467, 777
Cassinelli, J. P., Cohen, D. H., Macfarlane, J. J., et al. 1995, ApJ, 438, 932
Cassinelli, J. P., Cohen, D. H., Macfarlane, J. J., et al. 1996, ApJ, 460, 949
Caswell, J. L., Fuller, G. A., Green, J. A., et al. 2010, MNRAS, 404, 1029
Chan, S. J., Henning, T., & Schreyer, K. 1996, A&AS, 115, 285
Churchwell, E., Babler, B. L., Meade, M. R., et al. 2009, PASP, 121, 213
Clarke, A. J., Oudmaijer, R. D., & Lumsden, S. L. 2005, MNRAS, 363, 1111
Contreras, Y., Schuller, F., Urquhart, J. S., et al. 2013, A&A, 549, A45
Cooper, H. D. B., Lumsden, S. L., Oudmaijer, R. D., et al. 2013, MNRAS, 430, 1125
Cutri, R. M., Wright, E. L., Conrow, T., et al. 2012, Explanatory Sup-
    plement to the *WISE* All-Sky Data Release Products, http://wise2.ipac.
    caltech.edu/docs/release/allsky/expsup/index.html
Davies, B., Clark, J. S., Trombley, C., et al. 2012, MNRAS, 419, 1871
Davies, B., Hoare, M. G., Lumsden, S. L., et al. 2011, MNRAS, 416, 972
de Wit, W. J., Hoare, M. G., Oudmaijer, R. D., & Lumsden, S. L. 2010, A&A, 515, A45
Eder, J., Lewis, B. M., & Terzian, Y. 1988, ApJS, 66, 183
Egan, M. P., Price, S. D., Kraemer, K. E., et al. 2003, The Midcourse Space
    Experiment Point Source Catalog Version 2.3 Explanatory Guide, Air Force
    Research Laboratory Technical Report AFRL-VS-TR-2003-1589
Gallaway, M., Thompson, M. A., Lucas, P. W., et al. 2013, MNRAS, 430, 808
Gennaro, M., Brandner, W., Stolte, A., & Henning, T. 2011, MNRAS, 412, 2469
Green, J. A., Caswell, J. L., Fuller, G. A., et al. 2009, MNRAS, 392, 783
Green, J. A., Caswell, J. L., Fuller, G. A., et al. 2012, MNRAS, 420, 3108
Green, J. A., & McClure-Griffiths, N. M. 2011, MNRAS, 417, 2500
Guzmán, A. E., Garay, G., & Brooks, K. J. 2010, ApJ, 725, 734
Guzmán, A. E., Garay, G., Brooks, K. J., & Voronkov, M. A. 2012, ApJ, 753, 51
Hambly, N. C., Collins, R. S., Cross, N. J. G., et al. 2008, MNRAS, 384, 637
Helfand, D. J., Becker, R. H., White, R. L., Fallon, A., & Tuttle, S. 2006, AJ, 131, 2525
Hewett, P. C., Warren, S. J., Leggett, S. K., & Hodgkin, S. T. 2006, MNRAS, 367, 454
Hoare, M. G. 2006, ApJ, 649, 856
Hoare, M. G., & Franco, J. 2007, in Astrophysics and Space Science Proceed-
    ings, Diffuse Matter from Star Forming Regions to Active Galaxies—A
    Volume Honouring John Dyson, ed. T. W. Hartquist, J. M. Pittard, & S. A.
    E. G. Falle (Dordrecht: Springer), 61
Hoare, M. G., Purcell, C. R., Churchwell, E. B., et al. 2012, PASP, 124, 939
Hoare, M. G., Roche, P. F., & Glencross, W. M. 1991, MNRAS, 251, 584
Hodapp, K.-W. 1994, ApJS, 94, 615
Hodgkin, S., Irwin, M., Lewis, J., Gonzalez-Solares, E., & Yoldaş, A. K. 2012,
    in Astrophysics and Space Science Proceedings, Star Clusters in the Era of
    Large Surveys, ed. A. Moitinho & J. Alves (Berlin: Springer), 39
Hodgkin, S. T., Irwin, M. J., Hewett, P. C., & Warren, S. J. 2009, MNRAS, 394, 675

Hosokawa, T., & Omukai, K. 2009, ApJ, 691, 823
Hosokawa, T., Yorke, H. W., & Omukai, K. 2010, ApJ, 721, 478
Huenemoerder, D. P., Oskinova, L. M., Ignace, R., et al. 2012, ApJL, 756, L34
Kahn, F. D. 1974, A&A, 37, 149
Krticka, J., Korcakova, D., & Kubat, J. 2005, PAICz, 93, 29
Krumholz, M. R., Cunningham, A. J., Klein, R. I., & McKee, C. F. 2010, ApJ, 713, 1120
Krumholz, M. R., Klein, R. I., McKee, C. F., Offner, S. S. R., & Cunningham, A. J. 2009, Sci, 323, 754
Kuiper, R., Klahr, H., Beuther, H., & Henning, T. 2010, ApJ, 722, 1556
Kuiper, R., & Yorke, H. W. 2013, ApJ, 763, 104
Kurtz, S., Churchwell, E., & Wood, D. O. S. 1994, ApJS, 91, 659
Lanz, T., & Hubeny, I. 2007, ApJS, 169, 83
Larson, R. B. 1981, MNRAS, 194, 809
Lawrence, A., Warren, S. J., Almaini, O., et al. 2007, MNRAS, 379, 1599
Lépine, J. R. D., Cruz, P., Scarano, S., Jr., et al. 2011, MNRAS, 417, 698
Lewis, J. R., Irwin, M., & Bunclark, P. 2010, in ASP Conf. Ser. 434,
    Astronomical Data Analysis Software and Systems XIX, ed. Y. Mizumoto,
    K.-I. Morita, & M. Ohishi (San Francisco, CA: ASP), 91
Lucas, P. W., Hoare, M. G., Longmore, A., et al. 2008, MNRAS, 391, 136
Lumsden, S. L., Hoare, M. G., Oudmaijer, R. D., & Richards, D. 2002, MNRAS, 336, 621
Lumsden, S. L., Puxley, P. J., Hoare, M. G., Moore, T. J. T., & Ridge, N. A. 2003, MNRAS, 340, 799
Martins, F., Schaerer, D., & Hillier, D. J. 2005, A&A, 436, 1049
McKee, C. F., & Tan, J. C. 2003, ApJ, 585, 850
Minniti, D., Lucas, P. W., Emerson, J. P., et al. 2010, NewA, 15, 433
Mizuno, D. R., Carey, S. J., Noriega-Crespo, A., et al. 2008, PASP, 120, 1028
Molinari, S., Swinyard, B., Bally, J., et al. 2010, PASP, 122, 314
Moore, T. J. T., Urquhart, J. S., Morgan, L. K., & Thompson, M. A. 2012, MNRAS, 426, 701
Mottram, J. C., Hoare, M. G., Lumsden, S. L., et al. 2007, A&A, 476, 1019
Mottram, J. C., Hoare, M. G., Lumsden, S. L., et al. 2010, A&A, 510, A89
Mottram, J. C., Hoare, M. G., Davies, B., et al. 2011a, ApJL, 730, L33
Mottram, J. C., Hoare, M. G., Urquhart, J. S., et al. 2011b, A&A, 525, A149
Ortiz, R., Lorenz-Martins, S., Maciel, W. J., & Rangel, E. M. 2005, A&A, 431, 565
Pauldrach, A. W. A., Hoffmann, T. L., & Lennon, M. 2001, A&A, 375, 161
Price, S. D., Egan, M. P., Carey, S. J., Mizuno, D. R., & Kuchar, T. A. 2001, AJ, 121, 2819
Purcell, C. R., Hoare, M. G., Cotton, W. D., et al. 2013, ApJS, 205, 1
Reid, M. J., Menten, K. M., Zheng, X. W., et al. 2009, ApJ, 700, 137
Rygl, K. L. J., Brunthaler, A., Reid, M. J., et al. 2010, A&A, 511, A2
Schuller, F., Menten, K. M., Contreras, Y., et al. 2009, A&A, 504, 415
Shu, F. H., Adams, F. C., & Lizano, S. 1987, ARA&A, 25, 23
Skrutskie, M. F., Cutri, R. M., Stiening, R., et al. 2006, AJ, 131, 1163
Sridharan, T. K., Beuther, H., Schilke, P., Menten, K. M., & Wyrowski, F. 2002, ApJ, 566, 931
Thompson, M. A., Urquhart, J. S., Moore, T. J. T., & Morgan, L. K. 2012, MNRAS, 421, 408
Urquhart, J. S., Busfield, A. L., Hoare, M. G., et al. 2007a, A&A, 474, 891
Urquhart, J. S., Busfield, A. L., Hoare, M. G., et al. 2007b, A&A, 461, 11
Urquhart, J. S., Busfield, A. L., Hoare, M. G., et al. 2008, A&A, 487, 253
Urquhart, J. S., Hoare, M. G., Lumsden, S. L., et al. 2012, MNRAS, 420, 1656
Urquhart, J. S., Hoare, M. G., Purcell, C. R., et al. 2009, A&A, 501, 539
Urquhart, J. S., Moore, T. J. T., Hoare, M. G., et al. 2011a, MNRAS, 410, 1237
Urquhart, J. S., Moore, T. J. T., Schuller, F., et al. 2013a, MNRAS, 431, 1752
Urquhart, J. S., Morgan, L. K., Figura, C. C., et al. 2011b, MNRAS, 418, 1689
Urquhart, J. S., Thompson, M. A., Moore, T. J. T., et al. 2013b, MNRAS, in
    press (arXiv:1307.4105)
van Loo, S., Falle, S. A. E. G., & Hartquist, T. W. 2007, MNRAS, 376, 779
Wright, E. L., Eisenhardt, P. R. M., Mainzer, A. K., et al. 2010, AJ, 140, 1868